Research Square

Preprints are preliminary reports that have not undergone peer review.
They should not be considered conclusive, used to inform clinical practice,
or referenced by the media as validated information.

Process Optimization and Temperature-Dependent Kinetic Modeling of Reactive Oxygen and Nitrogen Species in Plasma Activated Water during Storage

Sofia Chanioti
Hellenic Agricultural Organization–DEMETER
Marianna Giannoglou
Hellenic Agricultural Organization–DEMETER
Panagiota Stergiou
Hellenic Agricultural Organization–DEMETER
Dimitrios Passaras
NCSR “Demokritos”
Panagiotis Dimitrakellis
NCSR “Demokritos”
George Kokkoris
National Technical University of Athens
Evangelos Gogolides
NCSR “Demokritos”
George Katsaros
gkatsaros@elgo.gr

Hellenic Agricultural Organization–DEMETER

Research Article

Keywords: Cold atmospheric plasma, Plasma activated water-PAW, Reactive oxygen and nitrogen species (RONS), Process optimization, Kinetic modeling, Storage stability

Posted Date: November 3rd, 2026

DOI: https://doi.org/10.21203/rs.3.rs-11228443/v1

License: This work is licensed under a Creative Commons Attribution 4.0 International License.
Read Full License

Additional Declarations: No competing interests reported.

Process Optimization and Temperature-Dependent Kinetic Modeling of Reactive Oxygen and Nitrogen Species in Plasma Activated Water during Storage

Sofia Chanioti[a], Marianna Giannoglou[a], Panagiota Stergiou[a], Dimitrios Passaras[b], Panagiotis Dimitrakellis,[b,c] George Kokkoris[b,d], Evangelos Gogolides[b], George Katsaros[a]*

[a] Institute of Technology of Agricultural Products, Hellenic Agricultural Organization–DEMETER, Lykovrissi 14123, Attica, Greece

[b] Institute of Nanoscience and Nanotechnology, NCSR "Demokritos", Agia Paraskevi 15341, Attiki, Greece

[c] Present address: Centre for Research and Technology Hellas / Chemical Process and Energy Resources Institute (CERTH/CPERI), 6th km Harilaou – Thermi, 57001 Thessaloniki, Greece

[d] School of Chemical Engineering, National Technical University of Athens, Zografou Campus, Zografou 15780, Athens, Greece

schanioti@gmail.com (https://orcid.org/0000-0001-9014-8735)
giannoglou@chemeng.ntua.gr (https://orcid.org/0000-0002-7633-8046)
ster.panagiota@gmail.com
d.passaras@inn.demokritos.gr
p.dimitrakellis@certh.gr (https://orcid.org/0000-0002-2601-8749)
gkokkoris@chemeng.ntua.gr (http://orcid.org/0000-0003-4507-7311)
e.gogolides@inn.demokritos.gr (http://orcid.org/0000-0002-1870-5629)
gkatsaros@elgo.gr (http://orcid.org/0000-0002-0090-2966)

*Corresponding author: Dr George Katsaros, Institute of Technology of Agricultural Products, Hellenic Agricultural Organisation-DEMETER, Sofokli Venizelou 1, Lykovrissi 14123, Attica, Greece, tel: +30-2102845940 (int.108)), e-mail: gkatsaros@elgo.gr

Abstract

The practical utilization of plasma-activated water (PAW) depends not only on the efficient generation of reactive oxygen and nitrogen species (RONS) but also on their preservation during storage. This study integrates process optimization with long-term kinetic modeling to characterize the effects of plasma processing conditions on RONS generation and predict their evolution in PAW during storage. PAW was produced using a helium atmospheric-pressure plasma jet, and the effects of nozzle-to-water surface distance, helium flow rate, discharge voltage, treatment time, and water volume were investigated using a five-factor Box–Behnken experimental design. Plasma processing conditions significantly affected RONS concentrations, pH, and electrical conductivity. The optimized conditions (16 min treatment time, 20 mL water volume, 4.3 mm nozzle-to-water distance, 6.4 kV discharge voltage, and 0.5 SLM helium flow rate) predicted H_2O_2 and NO_3^- concentrations of 29.93 and 14.40 mg L^{-1}, respectively, and an electrical conductivity of 386.07 μS cm^{-1}. In contrast, maximum NO_2^- production was predicted under different operating conditions, demonstrating a species-specific response to the plasma processing parameters. The long-term stability of PAW was subsequently evaluated for 105 days over a broad storage-temperature range (−80 to 25 °C). RONS losses were strongly dependent on both storage time and temperature. At −80 °C, H_2O_2, NO_2^-, and NO_3^- decreased by less than 10%, 11%, and 4%, respectively, during the first two weeks, whereas after more than 100 days the corresponding losses reached 48%, 31%, and 30%. A kinetic model describing the evolution of individual RONS during storage showed strong agreement between experimental and predicted concentrations. The derived kinetic parameters further demonstrated distinct temperature-dependent behavior under frozen and nonfrozen storage conditions. Overall, the integration of plasma-process optimization with

temperature-dependent kinetic modeling provides a quantitative framework for controlling RONS generation and predicting their persistence in PAW during long-term storage.

Keywords: Cold atmospheric plasma, Plasma activated water-PAW, Reactive oxygen and nitrogen species (RONS), Process optimization, Kinetic modeling, Storage stability

1. Introduction

Cold atmospheric plasma (CAP) has emerged as a powerful tool for modifying liquids, as plasma-exposed solutions often exhibit pronounced biological activity. This behavior originates from the transport of plasma-generated reactive oxygen and nitrogen species (RONS) across the gas–liquid interface into the liquid phase, where they initiate a cascade of chemical reactions [1]. When water is treated in this way, it becomes plasma-activated water (PAW), a chemically reactive solution characterized by altered pH and electrical conductivity and the accumulation of plasma-derived reactive species [2]. These species include highly reactive short-lived radicals, such as hydroxyl radicals, singlet oxygen and superoxide, as well as longer-lived compounds such as hydrogen peroxide, ozone, nitrite, nitrate and peroxynitrite formed through aqueous-phase reactions. Among these, long-lived RONS are particularly important because they can preserve part of the chemical reactivity generated by the plasma after treatment has ceased, thereby enabling PAW to exert effects beyond the point of its immediate production. The persistence of these long-lived species therefore plays an important role in determining the chemical reactivity and functional properties of PAW during subsequent use and storage.

Numerous studies have demonstrated that PAW is capable of inactivating bacteria and fungi on food surfaces, thereby contributing to shelf-life extension [3, 4, 5, 6, 7, 8, 9]. The antimicrobial

spectrum of PAW includes a wide range of microorganisms, such as *Escherichia coli, Candida albicans, Staphylococcus aureus, Listeria innocua, Aeromonas hydrophila, Pseudomonas fluorescens* and *Shewanella putrefaciens* [10, 11, 12, 13, 14]. Because of this broad biocidal activity, PAW has attracted interest as a disinfecting medium in food processing, agriculture, and industrial sanitation [11, 14, 15, 16, 17]. Importantly, PAW can be generated independently of its subsequent use, offering greater flexibility in its storage, transport, and integration into processes where direct plasma treatment or on-site generation may be impractical.

The chemical characteristics of PAW are commonly evaluated through measurements of pH and electrical conductivity (EC), together with direct quantification of relevant RONS. High EC values combined with acidic pH generally reflect the accumulation of ionic plasma-generated products, particularly nitrite and nitrate, alongside changes in the overall reactive-species composition [18]. Nevertheless, EC reflects the overall ionic composition of PAW rather than providing a direct measure of its total RONS concentration. However, the optimal composition of PAW depends strongly on its intended application. For instance, plant growth stimulation and seed germination may favor comparatively mild activation conditions with higher pH, low EC and limited RONS content [19], whereas microbial decontamination generally benefits from greater chemical reactivity, including low pH, high EC and high oxidant concentrations [20, 21, 22]. Consequently, careful control of RONS levels and physicochemical properties is essential to generate PAW with defined chemical characteristics.

The generation of PAW with tailored properties depends on multiple plasma and process parameters, including the plasma source and power, working gas composition, treatment duration, gas flow rate, liquid handling conditions and temperature [23, 24, 25, 26]. These parameters influence energy transfer to the gas phase, plasma–liquid interactions, and the subsequent

formation and transformation of reactive species in the aqueous phase. Because these variables interact in complex ways, multivariable optimization approaches such as response surface methodology (RSM) are particularly valuable for PAW production. Rather than simply maximizing treatment intensity, operating conditions can be optimized to achieve a target RONS composition and physicochemical profile and to identify species-specific responses to changes in plasma operating conditions.

The chemical stability of PAW during storage is a key factor for characterization, since its reactivity may evolve significantly over time. While several investigations have reported changes in individual RONS during storage, a consistent picture of their long-term, temperature-dependent behavior is still lacking. For instance, only minor variations in nitrate and hydrogen peroxide have been reported after two weeks of refrigerated storage [25], whereas storage at ambient temperature has been associated with pronounced nitrate depletion, reaching nearly 50% within three weeks [27]. Other studies have shown that hydrogen peroxide decreases gradually, with its stability strongly improved at lower temperatures, while nitrite and nitrate typically undergo faster early-stage decay [4]. In contrast, freezing conditions appear to preserve PAW reactivity much more effectively, as long-lived species remain largely unchanged for weeks at sub-zero temperatures and PAW stored at −80°C has been shown to retain strong antimicrobial activity even after prolonged storage [18, 28]. Frozen storage is therefore of particular interest because PAW can potentially be preserved not only as an activated liquid but also as plasma-activated ice, while substantially modifying the conditions under which aqueous-phase reactions and RONS degradation occur.

Despite the growing body of literature on plasma-activated water, most studies focus either on its immediate antimicrobial performance or on isolated storage conditions, without systematically

linking PAW stability to its plasma-generation parameters. In particular, there is limited quantitative understanding of how multiple plasma operating variables jointly determine the initial physicochemical and RONS profile of PAW and how this reactive-species profile subsequently evolves during storage. Moreover, existing stability studies typically examine short storage periods or a limited number of storage temperatures, restricting the ability to predict RONS availability under different time–temperature conditions. A quantitative description of these changes is particularly important because individual RONS may exhibit different formation and degradation behavior, and their persistence cannot necessarily be inferred from the initial physicochemical characteristics of PAW.

The present work addresses this gap by combining multivariate process optimization with long-term kinetic modeling of PAW RONS evolution. By integrating a five-factor response surface methodology with extended storage experiments across a wide temperature range, this study provides a predictive framework for describing the effects of plasma processing conditions on the initial PAW composition and predicting the subsequent persistence of individual long-lived RONS. Rather than considering PAW production and storage as independent stages, the proposed approach treats generation, preservation, and predicted availability of reactive species as interconnected elements of PAW process design. This integrated approach provides a quantitative basis for relating plasma operating conditions to RONS generation and for predicting the persistence of individual reactive species under different storage conditions.

In this work, plasma-activated water produced by a helium atmospheric-pressure plasma jet was systematically characterized in terms of RONS concentration, pH and electrical conductivity. The influence of key processing variables—including nozzle-to-water distance, helium flow rate, discharge voltage, treatment time and water volume—was evaluated using a five-factor Box–

Behnken experimental design. These parameters were optimized to maximize the concentrations of H_2O_2, NO_2^- and NO_3^- while controlling pH and EC. Because the conditions maximizing individual RONS were not necessarily identical, the optimization also enabled the identification of species-specific responses to the investigated plasma processing parameters. Finally, the stability of PAW produced under the selected optimized conditions was assessed over a 105-day period across storage temperatures ranging from −80 to 25 °C by monitoring changes in individual reactive species and developing kinetic models to predict their concentration as a function of storage time and temperature.

2. Materials and Methods

2.1 Plasma-Activated Water (PAW) Preparation

Plasma-activated water was generated using an atmospheric pressure plasma system located at the Institute of Nanoscience & Nanotechnology, NCSR "Demokritos" (Greece). Deionized (DI) water was enriched with reactive oxygen and nitrogen species (RONS) using a plasma jet reactor mounted on a supporting platform (Fig. 1). The reactor consisted of a glass tube with a nozzle positioned at adjustable distances above the water surface. Helium gas (He, 99.999%, Air Liquide Hellas) was supplied through a mass flow controller (GF40, Brooks). Plasma formation occurred by applying a high-voltage potential between a grounded electrode beneath the water container and a high-voltage electrode surrounding the glass tube near the nozzle. The supporting platform incorporated a high-voltage plasma generator (G2000, Redline Technologies), a voltage probe (PVM, North Star High Voltage), and an oscilloscope (DSO-X 3014A, Agilent Technologies) for real-time voltage monitoring. The plasma was operated with a sinusoidal voltage of 5–6.4 kV (peak-to-peak) at 82 kHz. Key processing parameters-including He flow rate, nozzle-to-water

distance, DI water volume, discharge voltage, and treatment duration-were systematically varied according to a Box–Behnken experimental design (Section 2.2).

2.2 Box–Behnken Experimental Design for Optimization of PAW Production

Response surface methodology (RSM) using a Box–Behnken design (BBD) was applied to optimize PAW production conditions [29]. Five independent factors were examined: nozzle-to-water distance (X_1 = 2.3, 3.3, 4.3 mm), He flow rate (X_2 = 0.5, 0.7, 1 SLM), discharge voltage (X_3 = 5, 5.7, 6.4 kV), treatment time (X_4 = 4, 10, 16 min), and water volume (X_5 = 20, 35, 50 mL). The experimental matrix consisted of 46 runs, including 40 factor combinations and six center-point replicates (Table 1).

The measured responses were H_2O_2, NO_2^-, and NO_3^- concentrations, pH, and electrical conductivity (EC). All experiments were conducted in randomized order to minimize uncontrolled variability.

Table 1. Design parameters for a five-way factorial Box-Behnken design of experiments.

Sr. No.	Variable	Code	Level		
1	Distance of the glass tube from the water surface (mm)	Dis	2.3(−1)	3.3(0)	4.3(1)
2	He Flow rate (SLM)	F_{HE}	0.5(−1)	0.7(0)	1(1)
3	Discharge voltage(kV)	Vol	5(−1)	5.7(0)	6.4(1)
4	Plasma treatment time (min)	Tp	4(−1)	10(0)	16(1)

5	Volume of the water sample (mL)	V	20(−1)	35(0)	50(1)

The response data were modeled corresponding to Box–Behnken design (Equation 1).

$$Y = \beta_0 + \sum_{i=1}^{5} \beta_i X_i + \sum_{i=1}^{5} \beta_{ii} {X_i}^2 + \sum_{i=1}^{4} \sum_{j=2}^{5} \beta_{ij} X_i X_j \quad \text{(Eq. 1)}$$

where Y represents the dependent variables (H_2O_2, NO_2^-, NO_3^-, pH, EC), β_0 is the intercept, β_i, β_{ii}, and β_{ij} are regression coefficients for linear, quadratic, and interaction terms, respectively. Statistical analyses were performed using Statistica 7.0 (Statsoft, USA). Model accuracy was assessed via the coefficient of determination (R^2) and lack-of-fit test, while the significance of coefficients was evaluated using ANOVA F-tests. Response surfaces and desirability profiles were plotted, and additional experiments were conducted to validate model predictions.

2.3 Storage Stability of Optimized PAW

PAW generated under optimized conditions was aliquoted into sterile glass containers (10 mL each) and stored at eight different temperatures: 25°C, 10°C, 4°C, 0°C (MIR-154 incubator, PHCbi), −12°C, −18°C, −24°C (standard freezer, Hisense), and −80°C (ultra-low temperature freezer, DW-HL218, Meiling Biology & Medical, China). Samples were periodically brought to room temperature, vortexed, and analyzed over a 105-day period to monitor H_2O_2, NO_2^-, NO_3^- concentrations, pH, and EC.

2.4 Physicochemical Characterization of PAW

H_2O_2 concentration was determined using the titanium sulfate assay [30] and compared against a standard curve (0–25 mg/L). NO_2^- and NO_3^- concentrations were measured following Merino (2009) [31], using standard curves for NO_2^- (0–6 mg/L). pH measurements were performed with

an ORION ion analyzer (EA 940, USA) at 25 ± 1°C, and EC was recorded using an ORION 150 HI-99300 meter (USA).

2.5 Data Analysis

All measurements were performed in triplicate, and results were expressed as mean ± standard deviation (SD). Statistical differences were assessed by one-way ANOVA followed by Duncan's test at $p < 0.05$.

During storage studies, H_2O_2, NO_2^-, and NO_3^- concentrations were plotted over time for each temperature. Kinetic modeling employed zero-order reaction equations (Equation 2).

$$C_i = C_{0,i} - k_i \cdot t \qquad \text{(Eq. 2)}$$

The effect of storage temperature on degradation rates was modeled using the Arrhenius equation (Equation 3).

$$lnk_i = lnA_i - \frac{E_{a,i}}{R}\frac{1}{T} \qquad \text{(Eq. 3)}$$

Combined, Equations 2 and 3 predicted the concentration of reactive species in PAW during storage (Equation 4).

$$C_i = C_{0,i} - e^{\left(-\frac{E_{a,i}}{R}\frac{1}{T} + lnA_i\right)}t \qquad \text{(Eq. 4)}$$

where C_i and $C_{0,i}$ are concentrations at time $t$and $t = 0$, respectively; k_i is the rate constant, T is storage temperature (K), $E_{a,i}$ is activation energy (J/mol), R is the universal gas constant (8.314 J/mol·K), A_i is the frequency factor, and $i$represents H_2O_2, NO_2^-, or NO_3^-.

3. Results and Discussion

As PAW production by an atmospheric pressure plasma jet (APPJ) is generally a multi-parameter process, the selection and optimization of experimental conditions represent a critical step in the production of PAW with controlled RONS concentrations and physicochemical characteristics. In the present study, response surface methodology (RSM) was applied to evaluate and optimize the processing parameters for PAW production by an APPJ. Therefore, the effects of the distance of the glass tube nozzle from the water surface (Dis), the flow rate of He (F_{HE}), the discharge voltage (VOL), the plasma treatment time (Tp), and the water sample volume (V) were examined. The results of 46 runs using a Box-Behnken design are given in Table 1, including the experimental design and the corresponding response data.

The results showed that the concentration of H_2O_2 in PAW ranged from 0.94 to 26.22 mg/L. The maximum experimentally measured concentration of H_2O_2 was found under the experimental conditions of DIS = 3.3 mm, F_{He} = 0.7 SLM, VOL = 5.7 kV, Tp = 16 min, and V = 20 mL. The concentration of NO_3^- in PAW ranged from 0.96 to 12.97 mg/L and the maximum experimentally measured concentration was also found under the same conditions, i.e., DIS = 3.3 mm, F_{He} = 0.7 SLM, VOL = 5.7 kV, Tp = 16 min, and V = 20 mL. Furthermore, the concentration of NO_2^- in PAW ranged from 0.44 to 4.22 mg/L and the maximum experimentally measured concentration was found under the conditions DIS = 3.3 mm, F_{He} = 0.5 SLM, VOL = 5.7 kV, Tp = 10 min, and V = 50 mL. The different experimental conditions associated with the highest NO_2^- concentration compared with those producing the highest H_2O_2 and NO_3^- concentrations indicate that the accumulation of individual long-lived RONS responds differently to changes in the APPJ processing conditions.

Several researchers have investigated the concentration of H_2O_2, NO_2^-, and NO_3^- in PAW and demonstrated that the processing parameters affect the concentration of RONS. Shen et al. (2016)

[28] estimated the concentration of H_2O_2, NO_2^-, and NO_3^- formed in PAW to be approximately 0.76 mg/L, 1.21 mg/L, and 41 mg/L, respectively, after 20 min treatment by an APPJ operated with air. Sajib et al. (2020) [23] reported that the values of H_2O_2 and NO_2^- concentrations were 8.50 mg/L and 0.40 mg/L after 15 min of air plasma processing, respectively. The differences between these reported concentrations and those obtained in the present study are expected, since RONS generation in PAW is strongly dependent on the plasma configuration, working gas, discharge conditions, treatment time, liquid volume, and gas–liquid interaction conditions. pH and EC values of PAW ranged from 4.83 to 2.85 and from 23.5 to 285 μS/cm, respectively.

PAW with the lowest pH and highest conductivity values was produced under the conditions of DIS = 3.3 mm, F_{He} = 0.7 SLM, VOL = 5.7 kV, Tp = 16 min and V = 20 mL. The values of pH and EC were within the ranges reported in the literature (pH values: 2.3-3.2, [14], [28], [32], [33], and conductivity values: 17-450 μS/cm, [12], [34]). The coincidence of high H_2O_2 and NO_3^- concentrations with increased EC and decreased pH under these conditions is consistent with the progressive accumulation of plasma-generated reactive and ionic species in the treated water. However, EC should be interpreted as an indicator of changes in the ionic composition of PAW rather than as a direct measure of total RONS, since neutral species such as H_2O_2 do not directly contribute to conductivity. Therefore, optimum process conditions should be investigated in order to obtain a targeted combination of H_2O_2, NO_2^-, and NO_3^- concentrations and physicochemical properties in PAW after plasma treatment.

3.1 Model Fitting

The regression coefficients of the linear and quadratic terms and the interaction terms between the variables of the model are presented in Table 2. It was observed that the concentration of H_2O_2 was mainly affected by the linear terms of the He flow rate (F_{HE}), the discharge voltage (VOL), the plasma treatment time (Tp), and the water sample volume (V). In addition, the variables with the greatest effect on NO_2^- concentration were the linear terms of plasma treatment time (Tp), the water sample volume (V), and the interactions of the model variables. The dominant effect in the model developed for NO_3^- concentration was also determined by the linear terms of He flow rate (F_{HE}), the discharge voltage (VOL), the plasma treatment time (Tp), and the water sample volume (V). These differences further indicate that the formation and accumulation of individual RONS are governed by distinct responses to the investigated plasma and liquid-phase processing conditions.

It can be observed that quadratic and linear terms of He flow rate (F_{HE}, F_{HE}^2), of discharge voltage (VOL, VOL^2), of plasma treatment time (Tp, Tp^2), and the linear term of water sample volume (V) had the strongest effect ($p<0.001$) in the developed pH model, followed by the quadratic term of the distance of the glass tube nozzle from the water surface (DIS^2), and the interaction term of DIS × F_{HE}. The variables with the greatest effect on conductivity of PAW were the linear terms of He flow rate (F_{HE}), discharge voltage (VOL), plasma treatment time (Tp), and water sample volume (V), followed by the quadratic term of water sample volume (V^2), and the linear term of the distance of the glass tube nozzle from the water surface (DIS). Overall, treatment time, discharge voltage, He flow rate, and water volume emerged as the principal variables governing PAW chemistry, whereas nozzle-to-water distance exerted a comparatively more limited response-dependent effect.

Relatively high F values and low significance values ($p<0.001$) indicate that the models are statistically significant. The R^2 values were 0.9447, 0.8766, 0.9077, 0.9290 and 0.9216 for H_2O_2, NO_2^-, NO_3^-, pH and conductivity in PAW, respectively (Table 2), indicating that the models adequately represented the relationships between the selected processing parameters and the corresponding responses. Thus, the models explained approximately 94.5%, 87.7%, 90.8%, 92.9%, and 92.2% of the observed variability in H_2O_2, NO_2^-, NO_3^-, pH, and conductivity, respectively. The comparatively high coefficients of determination across all five responses support the use of the developed models for examining the combined effects of the investigated APPJ operating and liquid-processing parameters within the experimental domain. The fitted surface models for H_2O_2, NO^{2-}, and NO^{3-} concentrations, and pH and conductivity in PAW are given in Eqs. (5), (6), (7), (8) and (9), respectively.

$$[H_2O_2] = 6.57 - 1.49F_{HE} + 2.90VOL + 5.13Tp - 5.02V + 3.00V^2 - 1.94\,VOLV - 3.96\,TpV \quad \text{(Eq. 5)}$$

$$[NO_2^-] = 3.40 - 1.06T^2 + 0.30V - 0.40V^2 + 0.78F_{HE}VOL + 0.78F_{HE}Tp - 1.10F_{HE}V - 1.16VOLTp + 1.18VOLV + 1.39TpV \quad \text{(Eq. 6)}$$

$$[NO_3^-] = 2.54 - 1.29F_{HE} + 1.85VOL + 2.11Tp - 1.92V + 1.12V^2 - 2.59VOLV - 1.94TpV \quad \text{(Eq. 7)}$$

$$[pH] = 3.25 + 0.21DIS^2 + 0.27\,F_{HE} + 0.32\,F_{HE}^2 - 0.36VOL + 0.29VOL^2 - 0.53Tp + 0.44Tp^2 + 0.38V - 0.31DISF \quad \text{(Eq. 8)}$$

$$[EC] = 109.60 + 14.32DIS - 34.95F_{HE} + 46.84VOL + 64.01Tp - 56.09V + 24.78V^2 - 32.48\,F_{HE}VOL \quad \text{(Eq. 9)}$$

308 **Table 2.** Regression coefficients and analysis of variance for the response surface of H_2O_2,

309 NO_2^-, NO_3^- concentrations, pH, and EC values of PAW

	Concentration of H_2O_2 (mg/L)			
	A Regression coefficients		**B Analysis of variance (ANOVA)**	
	COEFF[a]	**SE[a]**	**SS[b]**	**F-value**
Model	6.57	0.68	1202.57	21.17***
F_{HE}	-1,49	0.42	35.46	12.48***
VOL	2,90	0.42	134.91	47.51***
Tp	5,13	0.42	420.35	148.01***
V	-5.02	0.42	403.00	141.91***
V^2	2.92	0.57	74.48	26.22***
VOLV	-1.94	0.84	15.05	5.30*
TpV	-3.96	0.84	62.73	22.08***
Residual			70.99	
Lack of fit			70.18	0.058
Total			1273.56	

	Concentration of NO_2^- (mg/L)			
	A Regression coefficients		**B Analysis of variance (ANOVA)**	
	COEFF[a]	**SE[a]**	**SS[b]**	**F-value**
Model	3.40	0.20	44.24	8.88***
Tp	-1.06	0.16	9.89	39.72***
V	0.30	0.12	1.41	5.66*

V^2	-0.40	0.17	1.38	5.58*
$F_{HE}VOL$	0.78	0.25	2.42	9.71**
$F_{HE}Tp$	0.78	0.25	2.42	9.71**
$F_{HE}V$	-1.10	0.25	4.82	19.34***
VOLTp	-1.16	0.25	5.40	21.71***
VOLV	1.18	0.25	5.59	22.45***
TpV	1.39	0.25	7.67	30.80***
Residual			6.22	
Lack of fit			6.12	0.072
Total			50.46	

	Concentration of NO_3^- (mg/L)			
	A Regression coefficients		**B Analysis of variance (ANOVA)**	
	COEFF[a]	**SE[a]**	**SS[b]**	**F-value**
Model	2.67	0.64	290.07	5.85***
F_{HE}	-1.29	0.39	26.54	10.72***
VOL	1.72	0.39	47.51	19.16***
Tp	2.23	0.39	79.88	32.24***
V	-1,91	0.39	58.71	23.70***
VOLV	-2,10	0.78	17.68	7.13**
TpV	-2.43	0.78	23.62	9.53**
Residual			61.96	
Lack of fit			61.62	0.096
Total			352.03	

	pH			
	A Regression coefficients		B Analysis of variance (ANOVA)	
	COEFF[a]	SE[a]	SS[b]	F-value
Model	3.24	0.12	13.44	7.88***
DIS^2	0.21	0.09	0.38	4.48*
F_{HE}	0.27	0.07	1.16	13.57***
F_{HE}^2	0.32	0.09	0.91	10.64**
VOL	-0.37	0.07	2.14	25.08***
VOL^2	0.29	0.09	0.74	8.62**
Tp	-0.53	0.07	4.53	53.06***
Tp^2	0.44	0.09	1.68	19.68***
V	0.38	0.07	2.32	27.23***
DISF	-0.31	0.15	0.39	4.57*
Residual			2.13	
Lack of fit			2.12	0.081
Total			15.58	

	Conductivity (µS/cm)			
	A Regression coefficients		B Analysis of variance (ANOVA)	
	COEFF[a]	SE[a]	SS[b]	F-value
Model	109.60	10.49	194061.4	14.70***
DIS	14.32	6.42	3283.3	4.97*
F_{HE}	-34.99	6.42	19586.0	29.67***
VOL	46.85	6.42	35117.8	53.20***

Tp	64.02	6.42	65571.8	99.34***
V	-56.09	6.42	50347.5	76.27***
V^2	24.79	8.69	5361.3	8.12**
$F_{HE}VOL$	-32.48	12.85	4218.5	6.39**
Residual			16502.2	
Lack of fit			16390.0	0.278
Total			210563.6	

a COEFF: Coefficients, SE: Standard error b SS: Sum of Squares * P<0,05, ** P<0,01, *** P<0,001

3.2 Interpretation of response surface model and contour plots

The relationship between independent and dependent variables was illustrated using 3D response surface plots and 2D contour plots generated from the developed models for the concentrations of H_2O_2, NO_2^-, and NO_3^- as well as for the pH and EC values in PAW (Figs. 2-6). The plots were generated by varying two variables within their experimental range while keeping the remaining variables constant at their central levels. These response surfaces provide insight into the individual and combined effects of the APPJ operating conditions on the accumulation of long-lived RONS and the resulting physicochemical characteristics of PAW.

As it can be seen in Fig. 2a, a decrease in He flow from 1 to 0.5 SLM (for a 3.3 mm distance of the glass tube from the water surface) promoted an increase in the concentration of H_2O_2 from 2.19 to 7.87 mg/L. This inverse relationship indicates that, under the conditions investigated, lower He flow rates favored H_2O_2 accumulation in the liquid phase. Gas flow rate can influence both the plasma characteristics and the interaction of the plasma effluent with ambient air, thereby affecting the formation and transport of reactive species to the liquid [35]. Girard et al. (2016) [36] reported

that the concentration of H_2O_2 in PAW was higher at lower gas flow rates. At lower flow rates, greater interaction of the plasma effluent with ambient air may occur, potentially modifying the production of oxygen- and nitrogen-containing reactive species and their subsequent transfer to the liquid. Conversely, increasing the gas flow rate increases the velocity of the working gas and may reduce the residence time available for gas-phase reactions and plasma-effluent/ambient-air interactions, thereby influencing the reactive-species flux reaching the liquid [37]. Further, the application of higher voltages (at 20 mL volume, 0.7 SLM and 3.3 mm distance) promoted an increase in the concentration of H_2O_2 from 8.21 to 22.42 mg/L (Figure 2b). This behavior may be associated with enhanced energy input into the discharge at higher voltage, promoting the generation of reactive species and ultimately H_2O_2 accumulation in the liquid phase. At a discharged voltage of 6.4 kV and a volume of 35 mL, an increase in the plasma treatment time from 4 to 16 min promoted an increase in H_2O_2 concentration from 3.33 to 16.53 mg/L (Fig. 2c and d). This is in general agreement with the studies of Girard et al. (2016) [36] and Ghimire et al. (2021) [35] who also reported that increasing the treatment time increased the accumulation of H_2O_2 in PAW, with concentrations ranging from hundreds of micromolar to millimolar levels depending on the plasma system and operating conditions. The positive effect of treatment time reflects the cumulative generation and transfer of reactive oxygen species into the liquid, provided that H_2O_2 formation exceeds its simultaneous consumption through plasma-induced reactions. Thus, the observed H_2O_2 concentration represents the net balance between its plasma-induced formation and its concurrent consumption in the liquid phase rather than simply the cumulative plasma exposure. The distance of the glass tube nozzle from the water surface did not appear to significantly affect the concentration of H_2O_2 in the PAW within the experimental range investigated.

Fig. 3a shows the interaction between the He flow rate and the distance of the glass tube from the water surface on the concentration of NO_2^- at fixed discharge voltage, treatment time, and water volume of 5.7 kV, 10 min and 35 mL, respectively. The linear effect of He flow on the concentration of NO_2^- was clear from Figs. 3 a and c, as a decrease in the He flow rate and an increase in treatment time were reflected by an increase in the concentration of NO_2^- over the investigated experimental range. For instance, by applying a distance of the glass tube nozzle from the water surface of 2.3 mm, the reduction of the flow of He from 1 to 0.5 SLM caused an increase in the concentration of NO_2^- from 2.29 to 3.57 mg/L. As observed for H_2O_2, this response suggests that lower He flow favored the formation and/or transfer of reactive species involved in aqueous NO_2^- formation. Since He was used as the working gas, the formation of nitrogen-containing species necessarily involves interaction of the plasma effluent with nitrogen- and oxygen-containing species from the surrounding atmosphere and their subsequent transfer and reaction at the gas–liquid interface. The concentration of NO_2^- increased with increasing the discharge voltage and the plasma treatment time and almost reached a maximum at the longest distance of the glass tube nozzle from the water surface (~4.02 mg/L) (Figure 3d). The plasma treatment time had a quadratic effect on the concentration of NO_2^- which reached the highest value (~4.22 mg/L) at 0.5 SLM, 5.7 kV, and 50 mL. The nonlinear dependence on treatment time is consistent with the transient nature of NO_2^- in PAW, since its concentration represents the balance between its continuous formation and its subsequent participation in secondary aqueous-phase reactions. This behavior contrasts with the more consistently increasing H_2O_2 response and further demonstrates the species-dependent chemistry occurring during plasma activation of water.

Regarding the concentration of NO_3^- in PAW, a decrease in the flow of He from 1 to 0.5 SLM (for a 3.3 mm distance of the glass tube from the water surface) increased the concentration of NO_3^-

372 from 3.33 to 8.09 mg/L (Fig. 4a). The concentration of NO_3^- was not significantly affected by the
373 distance of the glass tube nozzle from the water surface within the investigated range. Furthermore,
374 the application of higher voltages (at 20 mL volume, 0.7 SLM, and 3.3 mm distance) increased the
375 concentration of NO_3^- from 1.79 to 10.97 mg/L (Figure 4b). The concentration of NO_3^- increased
376 from 2.82 to 9.32 mg/L with increasing plasma treatment time (Figures 4c and 4d). Similarly, Risa
377 Vaka et al. (2019) [38] reported a significant increase ın the yield of these reactive nitrogen species
378 in PAW with increasing discharge voltage and exposure time. The similar positive effects of
379 discharge voltage and treatment time on H_2O_2 and NO_3^- indicate that these parameters are major
380 drivers of the accumulation of long-lived RONS in the present APPJ system. The maximum
381 concentration of NO_2^- achieved in PAW was significantly lower than the corresponding
382 concentration of NO_3^- despite their similar evolution regarding treatment duration and discharge
383 voltage. This could be attributed to the fact that NO_2^- is less stable under acidic conditions, where
384 protonation to nitrous acid (HNO_2) facilitates subsequent reaction pathways that can contribute to
385 NO_3^- formation and the release of nitrogen oxides[39]. Therefore, the relative concentrations of
386 NO_2^- and NO_3^- reflect not only their plasma-induced formation but also subsequent nitrogen-
387 species conversion reactions in the acidified aqueous phase. Tian et al. (2015) [24] confirmed a
388 higher concentration of NO_3^- (about 5 mg/L) compared with that of NO_2^- (only traces, <0.012
389 mg/L) after 20 min of plasma activation.

390 The pH of PAW exhibited a minimum within a He flow range of 0.5–0.7 SLM and a glass tube-
391 to-water surface distance of 2.3–3.3 mm, at a fixed water volume of 35 mL, a discharge voltage of
392 5.7 kV, and a treatment time of 10 min (Figure 5a). Dimitrakellis et al. (2021) [4] also reported
393 that the pH of PAW decreased with decreasing He flow from 5 to 1 SLM. According to the
394 interaction between the volume of water and voltage shown in Fig. 5b at a fixed treatment time of

10 min, He flow rate of 0.7 SLM and distance of 3.3 mm, the pH decreased with decreasing water volume and increasing discharge voltage and the minimum value was obtained for a water volume of 20 mL and voltage of 6.4 kV. Han et al. (2022) [10] also confirmed that the pH of PAW increased with increasing water volume from 20 to 50 mL, indicating greater dilution of plasma-generated acidifying species at the higher liquid volume under otherwise comparable processing conditions. Further, the He flow rate and treatment time had a clear quadratic effect on the pH of PAW, which reached the lowest value at 0.5 SLM and 16 min, respectively (Figure 5c). As the plasma interaction time with water increased, a significant decrease in pH ($p < 0.05$) was observed, as shown in Figs. 5(c) and 5(d). This may be associated with the progressive formation and accumulation of acidic and ionic species in PAW, arising from plasma-induced aqueous-phase chemistry. The obtained results concerning the control of plasma treatment time in order to achieve PAW with increased concentrations of reactive species and decreased pH are consistent with previous studies [17, 18, 22, 25, 39]. Similarly, the discharge voltage and treatment time showed a clear quadratic effect on the pH of PAW, and the minimum value was obtained at a voltage of 6.4 kV, and a treatment time of 16 min (Figure 5d). Han et al. (2022) [10] similarly reported a significant reduction in the pH of PAW when the plasma discharge voltage increased from 7.4 to 15.2 kV ($p < 0.05$). Hence, the lower pH observed at higher discharge voltage may be associated with enhanced formation and accumulation of acidifying plasma-generated species in the liquid phase. The simultaneous decrease in pH and increase in NO_3^- with increasing voltage and treatment time are therefore consistent with progressively enhanced nitrogen-species chemistry under more intensive plasma exposure, although pH cannot be attributed to any single measured RONS.

As can be seen in Fig. 6a, the EC of PAW increased with decreasing the He flow from 1 to 0.5 SLM at all tested distances of the glass tube from the water surface. A low flow rate had a greater impact on EC than higher flow rates. This indicates that lower He flow favored the accumulation of ionic species in PAW, resulting in higher EC values. This trend may be associated with greater admixture of ambient air into the plasma jet channel at lower gas flow rates, which can modify gas-phase RONS formation and their subsequent transfer into the liquid [32]. Concerning the influence of water volume and discharge voltage shown in Fig. 6b, the EC of PAW increased with decreasing water volume and increasing discharge voltage. Rathore & Nema (2021) [25] also reported lower PAW reactivity and EC with increasing water volume from 50 to 200 mL. This could be due to the fact that increasing the water volume dilutes the plasma-generated ionic and reactive species under otherwise similar processing conditions, resulting in higher pH and lower EC values. Furthermore, the He flow rate and treatment time had a clear linear effect on the EC of PAW (Figure 6c). Previous reports showed that PAW exhibited a significant increase in EC with increasing plasma activation time, which was attributed to the progressive accumulation of charged and ionic species in the liquid phase [4, 25]. Similarly, the discharge voltage and treatment time showed clear linear effects on the EC of PAW, and the maximum value was obtained at a voltage of 6.4 kV and a treatment time of 16 min (Figure 6d). Higher EC values were observed at higher voltages. This increase in EC is consistent with greater accumulation of plasma-generated ionic species at higher discharge voltages; however, EC should be interpreted as an indicator of the ionic composition of PAW rather than as a direct measure of total RONS concentration [19]. Taken together, the EC and pH responses complement the direct RONS measurements by demonstrating the broader physicochemical changes induced in the liquid as a function of the APPJ operating conditions.

3.3 Optimization of RONS production

To determine the processing conditions associated with the targeted PAW responses, the maximum concentrations of H_2O_2, NO_2^- and NO_3^- and EC, as well as the minimum pH, in PAW were determined by using a desirability function (ranging from 0 to 1, with values approaching 1 representing increasingly desirable conditions). It was observed that the maximum predicted concentration of H_2O_2 (29.93 mg/L) was achieved with a plasma treatment time of 16 min, water sample volume of 20 mL, distance of the glass tube from the water surface of 4.3 mm, discharge voltage of 6.4 kV and He flow rate of 0.5 SLM. Further, the maximum predicted NO_2^- concentration of 4.70 mg/L was obtained at a treatment time of 16 min, water volume of 50 mL, distance of the glass tube nozzle from the water surface of 4.3 mm, discharge voltage of 5 kV and He flow rate of 0.5 SLM. The maximum predicted value of the NO_3^- concentration was 14.40 mg/L which was obtained at a treatment time of 16 min, water sample volume of 20 mL, distance of the glass tube nozzle from the water surface of 4.3 mm, discharge voltage of 6.4 kV, and He flow rate of 0.5 SLM. Thus, the predicted conditions maximizing H_2O_2 and NO_3^- were identical, whereas maximum NO_2^- accumulation required a higher water volume and lower discharge voltage. This difference demonstrates that the APPJ operating conditions do not affect all long-lived RONS uniformly and that optimization of PAW production is dependent on the specific reactive species being targeted.

The minimum predicted pH value of PAW was 2.71, which was obtained at a treatment time of 16 min, water sample volume of 20 mL, distance of the glass tube nozzle from the water surface of 3.3 mm, discharge voltage of 6.4 kV, and He flow rate of 0.7 SLM. The maximum predicted value of PAW conductivity was 386.07 μS/cm, which was obtained at a treatment time of 16 min, a

water volume of 20 mL, a distance of the glass tube nozzle from the water surface of 4.3 mm, a discharge voltage of 6.4 kV, and a He flow rate of 0.5 SLM. Notably, the conditions maximizing EC coincided with those maximizing H_2O_2 and NO_3^-, consistent with the response-surface trends described above. In contrast, the conditions producing the minimum predicted pH differed slightly, particularly with respect to nozzle-to-water distance and He flow rate, further indicating that the physicochemical responses of PAW cannot be represented by a single common optimum.

The values of pH and EC were strongly correlated with concentrations of H_2O_2 ($r = -0.73$ and 0.87 for pH and EC, respectively; $p < 0.05$) and NO_3^- ($r = -0.63$ and 0.75 for pH and EC, respectively; $p < 0.05$) in PAW. Thus, increasing H_2O_2 and NO_3^- concentrations were associated with decreasing pH and increasing EC. These correlations are consistent with the simultaneous development of reactive and ionic species during plasma–liquid interaction. Nevertheless, these relationships should be interpreted as correlations within the investigated experimental system rather than as direct quantitative measures of RONS concentration. In particular, H_2O_2 is electrically neutral and therefore does not directly contribute to EC, whereas conductivity reflects the collective contribution of ionic species present in PAW.

Finally, to validate the model predictions, experiments were conducted using the optimized parameters for each individual response. Table 3 presents the variable levels optimized for each response and the values for the remaining responses derived either from the model or experimentally. The experimental values did not show significant differences compared with the corresponding predicted ones, indicating that the developed models were reliable and adequately described the responses within the investigated experimental domain. The agreement between predicted and experimental values therefore confirms the suitability of the developed RSM models for selecting PAW production conditions according to the targeted RONS composition and

physicochemical characteristics. Importantly, the response-specific optima demonstrate that the developed models can be used not only to maximize overall plasma-induced chemical modification of water but also to select processing conditions favoring different long-lived RONS profiles.

490

491 **Table 3.** Predicted and experimental values for the rest responses at optimum conditions of each response.

Process variables					Predicted values					Experimental values[a]				
X1 (mm)	X2 (SLM)	X3 (kV)	X4 (min)	X5 (mL)	$[H_2O_2]$ (mg/L)	$[NO_2^-]$ (mg/L)	$[NO_3^-]$ (mg/L)	pH	EC (µS/cm)	$[H_2O_2]$ (mg/L)	$[NO_2^-]$ (mg/L)	$[NO_3^-]$ (mg/L)	pH	EC (µS/cm)
4.3	0.5	6.4	16	20	29.93	3.98	14.40	3.28	386.07	31.96±0.85	3.86±0.12	15.24±0.87	3.07±0.10	388.69±1.54
4.3	0.5	5.0	16	50	6.17	4.70	2.98	4.76	109.25	6.05±0.21	4.61±0.18	2.02±0.57	4.89±0.09	108.07±1.25
3.3	0.7	6.4	16	20	28.44	2.08	13.11	2.71	304.32	29.87±0.52	2.82±0.42	14.01±0.74	2.66±0.09	306.01±1.88

492 [a] Mean of triplicate determination

493

3.4 Stability of PAW during storage

By applying selected optimized conditions for PAW production, PAW was obtained with the following physicochemical characteristics: H_2O_2 concentration of 29.63 mg/L, NO_2^- concentration of 3.90 mg/L, and NO_3^- concentration of 15.20 mg/L. These experimentally obtained concentrations were close to the values predicted by the optimization models, further supporting the adequacy of the developed models. PAW was stored at various temperatures (nonfrozen storage: 0, 4, 10, and 25 °C; frozen storage: -12, -18, -24 and -80 °C) and the changes in the concentrations of H_2O_2, NO_2^- and NO_3^- were evaluated during storage.

During a 105-day storage period, a significant decrease in the concentration of H_2O_2 in PAW was observed, estimated as 42%, 39%, 36%, 29%, 26%, 24%, 22%, and 16% of the initial concentration after 35 days at 25, 10, 4, 0, -12, -18, -24, and -80°C, respectively ($p < 0.05$) (Figures 7a and b); moreover, decreases of 93%, 85%, 76%, 71% 69%, 65%, 57%, and 48% in H_2O_2 concentration were observed, respectively, by the end of the storage period. These results demonstrate a clear temperature dependence of H_2O_2 stability, with progressively greater preservation as the storage temperature decreased. The rate of H_2O_2 concentration decrease followed the order: k(-80°C) < k(-24°C) < k(-18°C) < k(-12°C) ≈ k(0°C) < k(4°C) < k(10°C) < k(25°C) (Table 4). The lower rate constants under frozen conditions indicate that low-temperature storage effectively slows the reactions responsible for H_2O_2 depletion in PAW. This behavior is consistent with reduced molecular mobility and slower reaction kinetics at decreasing temperatures, although the observed H_2O_2 loss represents the net result of multiple reactions occurring within the PAW chemical system. Similar results were obtained by Tsoukou et al. (2020) [41] who reported that the concentrations of RONS, including H_2O_2 were affected by storage at

different temperatures (4, −16, −80, and −150 °C) confirming that liquids stored at higher temperatures underwent more rapid depletion of reactive chemical species during storage.

The concentration of NO_2^- in PAW also decreased significantly throughout the 105-day storage period. After 13 days of storage at 25, 10, 4, 0, -12, -18, -24, and -80°C, this decrease was estimated as 37%, 31%, 25%, 22%, 20%, 18%, 15%, and 11% of the respective initial value, as shown in Figures 8a and b ($p < 0.05$). At the end of the storage period, reductions of approximately 95%, 76%, 58%, 53% 50%, 39%, 33%, and 31% of the initial NO_2^- concentration were observed, respectively. NO_2^- decreased continuously throughout storage, although the magnitude of the decrease was markedly reduced at lower temperatures. A similar trend was observed for NO_2^- during a 14-day storage period at 4°C by Rathore & Nema (2021) [25]. The rate of NO_2^- concentration decrease followed the order: k(-80°C) < k(-24°C) < k(-18°C) < k(-12°C) ≈ k(0°C) ≈ k(4°C) < k(10°C) < k(25°C) (Table 4). As observed for H_2O_2, the progressive reduction in the rate constant with decreasing temperature confirms that NO_2^- persistence is strongly controlled by storage temperature. The pronounced depletion of NO_2^- at higher temperatures is also consistent with its reactive and transient character in acidified PAW, where it can participate in secondary nitrogen-species chemistry during storage.

Similarly, the concentration of NO_3^- in PAW decreased significantly during storage. After 13 days of storage at 25, 10, 4, 0, -12, -18, -24, and -80°C, this decrease was estimated as 33%, 31%, 24%, 18%, 12%, 9%, 8%, and 4% of the respective initial value, as shown in Figures 9a and b ($p < 0.05$). At the end of the storage period, reductions of 99%, 90%, 75%, 65% 57%, 47%, 35%, and 30% of the initial NO_3^- concentration were observed, respectively. Ruamrungsri et al. (2023) [27] reported that NO_3^- concentration in PAW decreased by approximately 33.75%, 35.88%, and 49.09% after 7, 14, and 21 days at 27°C, respectively confirming that NO_3^- concentration generated in PAW

gradually decreased with increasing storage time. In contrast, NO_3^- exhibited considerably greater short-term stability under frozen conditions in the present study. The NO_3^- concentrations in PAW were comparatively stable for 13 days when PAW was stored at −18, −24, and −80°C since the reduction was found to be only 4-9% of the initial concentration. The findings are in agreement with those published by Subramanian et al. (2020) [18] who reported that the concentration of NO_3^- in PAW was almost stable for 2 weeks at −20°C. The comparatively high persistence of NO_3^- under frozen storage further demonstrates that individual long-lived RONS exhibit distinct storage behavior and that the reactive-species profile of PAW changes as a function of both storage time and temperature [32]. The rate of NO_3^- concentration decrease followed the order: k(-80°C) < k(-24°C) < k(-18°C) < k(-12°C) < k(0°C) < k(4°C) < k(10°C) ≈ k(25°C) (Table 4). The different rate-constant patterns observed for H_2O_2, NO_2^-, and NO_3^- further indicate that PAW should not be considered as a chemically static system during storage, since its RONS composition evolves in a species-specific manner.

Taken together, the kinetic behavior of H_2O_2, NO_2^-, and NO_3^- demonstrates that storage temperature is a major determinant of long-lived RONS persistence in PAW. Although all three species progressively decreased during storage, freezing substantially slowed their depletion, with −80 °C providing the greatest preservation over the investigated temperature range. The transition from nonfrozen to frozen storage therefore resulted in a distinct kinetic regime characterized by substantially slower depletion of the investigated long-lived RONS. Even after 75 days of storage at -80°C, the decreases in H_2O_2, NO_2^-, and NO_3^- concentrations were only 34%, 23%, and 20% of their initial values, respectively, demonstrating substantial preservation of the reactive-species profile over prolonged storage. These results refer specifically to the persistence of the measured

chemical species and should not be interpreted as direct evidence of preserved biological or antimicrobial activity.

The effect of storage temperature on the degradation rate constants of H_2O_2, NO_2^- and NO_3^- was further quantified using the Arrhenius relationship and expressed in terms of apparent activation energy (E_a) (Table 4). Concerning the rate constants of H_2O_2 concentration change, the apparent activation energy was calculated as 13.07 kJ/mol for the nonfrozen temperatures and 8.48 kJ/mol for the frozen temperatures, respectively (Eq. 3). Similarly, the apparent activation energy was found to be 26.52 kJ/mol (25.01 kJ/mol) for the nonfrozen temperatures and 16.37 kJ/mol (19.42 kJ/mol) for the frozen temperatures for the rate constants of NO_2^- (NO_3^-) concentration change, respectively. Thus, the apparent activation energies decreased from 13.07 to 8.48 kJ/mol for H_2O_2, from 26.52 to 16.37 kJ/mol for NO_2^-, and from 25.01 to 19.42 kJ/mol for NO_3^- when comparing the nonfrozen and frozen temperature regions.

For all three species, the apparent activation energies were lower within the frozen-temperature region than within the nonfrozen region, indicating a change in the temperature dependence of the degradation kinetics after freezing. Rather than representing activation energies of individual elementary reactions, these values should be regarded as apparent kinetic parameters describing the overall temperature dependence of RONS depletion within the complex PAW system. This distinction suggests that RONS evolution in frozen PAW cannot simply be extrapolated from kinetic behavior measured in the liquid state and supports separate consideration of frozen and nonfrozen storage regimes when predicting PAW stability. The observation of two distinct temperature-dependent kinetic regimes represents an important feature of the present model, particularly when predicting long-term changes in PAW composition across temperatures spanning the liquid and frozen states.

584

585 **Table 4.** Rate constants k (d^{-1}) of the H_2O_2, NO_2^-, and NO_3^- concentration in PAW and
586 activation energies (kJ/mol) of the chemical species of PAW during refrigerated and freezer
587 storage.

T (°C)	k (d^{-1})		
	H_2O_2	**NO_2^-**	**NO_3^-**
Refrigerated storage			
25	0.2467±0.0041[a]	0.0296±0.0017[a]	0.1459±0.0027[a]
10	0.2344±0.0051[b]	0.0241±0.0012[b]	0.1233±0.0017[b]
4	0.2035±0.0042[c]	0.0195±0.0012[c]	0.0981±0.0026[c]
0	0.1918±0.0046[d]	0.0185±0.0007[c]	0.0878±0.0027[d]
Freezer storage			
-12	0.1848±0.0055[d]	0.0177±0.0009[c]	0.0784±0.0024[e]
-18	0.1750±0.0056[e]	0.0141±0.0011[d]	0.0667±0.0028[f]
-24	0.1523±0.0053[f]	0.0123±0.0014[de]	0.0510±0.0026[g]
-80	0.1333±0.0057[g]	0.0115±0.0011[e]	0.0453±0.0016[h]
Ea (kJ/mol) refrigeration	13.07±1.2	26.52±2.2	25.01±2.4
Ea (kJ/mol) freezing	8.48±0.9	16.37±1.8	19.42±2.1

588

589 **3.5 Proposed mathematical models**

590 According to the above data obtained from PAW storage after optimization for maximum
591 concentration of H_2O_2, NO_2^-, and NO_3^-, a combinatorial mathematical equation can be derived to

592 determine the concentration of individual reactive species of PAW during storage (Equation 4).

593 Hence, the corresponding equations are presented below.

594 To determine the decrease in H_2O_2 concentration in PAW during refrigerated storage (0-25°C):

595 $$C_{H_2O_2} = C_{H_2O_2,0} - e^{\left(-1572.5\frac{1}{T}+4.0967\right)}t \qquad \text{(Eq. 10)}$$

596 To determine the decrease in H_2O_2 concentration in PAW during freezer storage (–12-–80°C):

597 $$C_{H_2O_2} = C_{H_2O_2,0} - e^{\left(-1052.2\frac{1}{T}+2.3541\right)}t \qquad \text{(Eq. 11)}$$

598 where $C_{H_2O_2,0}$= 6.57-1.49* F_{HE}+2.90*Vol+5.13*Tp-5.02*V+3.00*V^2-1.94*Vol*V -3.96*Tp*V

599 To determine the decrease in NO_2^- concentration in PAW during refrigerated storage (0-25°C):

600 $$C_{NO_2^-} = C_{NO_2^-,0} - e^{\left(-3189.5\frac{1}{T}+7.7556\right)}t \qquad \text{(Eq. 12)}$$

601 To determine the decrease in NO_2^- concentration in PAW during freezer storage (–12-–80°C):

602 $$C_{NO_2^-} = C_{NO_2^-,0} - e^{\left(-1969.2\frac{1}{T}+3.4895\right)}t, \qquad \text{(Eq. 13)}$$

603 where $C_{NO_2^-,0}$ = 3.40-1.06*Tp^2+0.30*V-0.40*V^2+0.78*F_{HE}*Vol+0.78*F_{HE}*Tp-1.10*F_{HE}*V-

604 1.16*Vol*Tp+1.18*Vol*V+1.39*Tp*V

605 To determine the decrease in NO_3^- concentration in PAW during refrigerated storage (0-25°C):

606 $$C_{NO_3^-} = C_{NO_3^-,0} - e^{\left(-3008.1\frac{1}{T}+8.7168\right)}t \qquad \text{(Eq. 14)}$$

607 To determine the decrease in NO_3^- concentration in PAW during freezer storage (–12-–80°C):

608 $$C_{NO_3^-} = C_{NO_3^-,0} - e^{\left(-2335.6\frac{1}{T}+6.4141\right)}t, \qquad \text{(Eq. 15)}$$

where $C_{NO_3^-,0}$=2.54-1.29*F_{HE} +1.85*Vol+2.11*Tp-1.92*V+1.12*V^2-2.59*Vol*V-1.94*Tp*V

where, T the storage temperature and t the storage time.

In order to assess the reliability of the proposed models, scatterplots of the predicted and observed values for H_2O_2, NO_2^-, and NO_3^- concentrations were generated (Figure 10). The initial concentrations in Equations 10-15 were optimal, 29.63, 3.90, and 15.20 mg/L, respectively. The satisfactory correlation of predicted and observed values indicates that the proposed mathematical models are reliable.

4. Conclusions

This study demonstrated that the physicochemical characteristics and long-lived RONS composition of plasma-activated water (PAW) can be systematically modulated through the operating conditions of a helium atmospheric-pressure plasma jet. Key physicochemical properties of PAW—including H_2O_2, NO_2^-, and NO_3^- concentrations, pH, and electrical conductivity (EC)—were systematically evaluated and optimized as a function of nozzle-to-water distance, helium flow rate, discharge voltage, treatment time, and water volume using response surface methodology. The predicted optimal conditions for generating PAW with maximum H_2O_2 and NO_3^- concentrations and EC were identified as: 16 minutes of plasma treatment, a water volume of 20 mL, a nozzle-to-water distance of 4.3 mm, a discharge voltage of 6.4 kV, and a helium flow rate of 0.5 SLM. However, the conditions maximizing NO_2^- differed, demonstrating that the reactive-species profile of PAW can be tailored through the selection of processing conditions according to the targeted response. These findings demonstrate that individual long-lived RONS

630 respond differently to changes in the investigated APPJ operating conditions and that PAW
631 production cannot be described by a single universal optimum for all reactive species.
632 Storage studies further revealed that freezing, particularly at −80°C, effectively preserved the
633 investigated long-lived RONS over extended periods. In contrast, higher nonfrozen storage
634 temperatures resulted in more pronounced reductions in RONS concentrations, demonstrating the
635 strong temperature dependence of their depletion kinetics. The temperature dependence of RONS
636 degradation was quantitatively described through kinetic rate constants and apparent activation
637 energies, with distinct kinetic behavior observed between frozen and nonfrozen storage regimes.
638 Even after 75 days at −80 °C, H_2O_2, NO_2^-, and NO_3^- losses were limited to 34%, 23%, and 20%,
639 respectively, demonstrating substantial preservation of long-lived reactive species during
640 prolonged frozen storage. Moreover, the lower apparent activation energies determined within the
641 frozen-temperature region compared with the nonfrozen region for all three species indicate a
642 change in their effective temperature dependence after freezing. Therefore, RONS evolution under
643 frozen conditions should be considered separately rather than extrapolated directly from kinetic
644 behavior in nonfrozen PAW.
645 Finally, predictive mathematical models were developed to describe PAW characteristics as a
646 function of the processing parameters and the evolution of individual reactive species as a function
647 of storage temperature and time. The integration of process optimization with temperature-
648 dependent kinetic modeling therefore provides a quantitative basis for selecting both PAW
649 production and storage conditions according to the reactive-species profile required after a defined
650 storage period. Overall, the present study establishes an integrated framework linking APPJ
651 processing conditions with initial PAW composition and the subsequent time- and temperature-
652 dependent persistence of individual long-lived RONS. This framework contributes to a more

quantitative understanding of PAW generation and storage and provides a basis for designing PAW with controlled and predictable reactive-species profiles.

Acknowledgement

Part of the results of this study was financially supported by the project NOVISH (http://novish.itap.com.gr) co-funded by the European Union-European Maritime and Fisheries Fund and the Hellenic Republic, Ministry of Rural Development and Food, General Secretariat of Rural Development and Food, within the framework of Maritime and Fisheries Fund 2014-2020.

References

1. Pârvulescu VI, Magureanu M, Lukes P (2012) Plasma chemistry and catalysis in gases and liquids. John Wiley & Sons., Hoboken, NJ

2. Thirumdas R, Kothakota A, Annapure U, et al (2018) Plasma activated water (PAW): Chemistry, physico-chemical properties, applications in food and agriculture. Trends Food Sci Technol 77:21–31. https://doi.org/10.1016/j.tifs.2018.05.007

3. Chanioti S, Giannoglou M, Stergiou P, et al (2023) Cold-Atmospheric-Plasma Activated-Ice as a cooling medium with antimicrobial properties: case study on fish fillet preservation. Food Res Int 112639. https://doi.org/10.1016/j.foodres.2023.112639

4. Dimitrakellis P, Giannoglou M, Xanthou ZM, et al (2021) Application of plasma-activated water as an antimicrobial washing agent of fresh leafy produce. Plasma Process Polym 18:2100030. https://doi.org/10.1002/ppap.202100030

5. Giannoglou M, Dimitrakellis P, Efthimiadou A, et al (2021) Comparative Study on the Effect of Cold Atmospheric Plasma, Ozonation, Pulsed Electromagnetic Fields and High-Pressure Technologies on Sea Bream Fillet Quality Indices and Shelf Life. Food Eng Rev 13:175–184. https://doi.org/10.1007/s12393-020-09248-7

6. Giannoglou M, Stergiou P, Dimitrakellis P, et al (2020) Effect of Cold Atmospheric Plasma processing on quality and shelf-life of ready-to-eat rocket leafy salad. Innov Food Sci Emerg Technol 66:102502. https://doi.org/10.1016/j.ifset.2020.102502

7. Liao X, Su Y, Liu D, et al (2018) Application of atmospheric cold plasma-activated water (PAW) ice for preservation of shrimps (Metapenaeus ensis). Food Control 94:307–314.

https://doi.org/10.1016/j.foodcont.2018.07.026

8. Muhammad AI, Chen W, Liao X, et al (2019) Effects of Plasma-Activated Water and Blanching on Microbial and Physicochemical Properties of Tiger Nuts. Food Bioprocess Technol 12:1721–1732. https://doi.org/10.1007/s11947-019-02323-w

9. Wang J, Han R, Liao X, Ding T (2021) Application of plasma-activated water (PAW) for mitigating methicillin-resistant Staphylococcus aureus (MRSA) on cooked chicken surface. LWT 137:110465. https://doi.org/10.1016/j.lwt.2020.110465

10. Han Q, He Z, Zhong C, et al (2022) The optimization of plasma activated water (<scp>PAW</scp>) generation and the inactivation mechanism of <scp>PAW</scp> on *Escherichia coli*. J Food Process Preserv 46:. https://doi.org/10.1111/jfpp.17120

11. El Shaer M, Eldaly M, Heikal G, et al (2020) Antibiotics Degradation and Bacteria Inactivation in Water by Cold Atmospheric Plasma Discharges Above and Below Water Surface. Plasma Chem Plasma Process 40:971–983. https://doi.org/10.1007/s11090-020-10076-0

12. Ma R, Wang G, Tian Y, et al (2015) Non-thermal plasma-activated water inactivation of food-borne pathogen on fresh produce. J Hazard Mater 300:643–651. https://doi.org/10.1016/j.jhazmat.2015.07.061

13. Chiappim W, Sampaio A da G, Miranda F, et al (2021) Antimicrobial Effect of Plasma-Activated Tap Water on Staphylococcus aureus, Escherichia coli, and Candida albicans. Water 13:1480. https://doi.org/10.3390/w13111480

14. Zhao Y -M., Ojha S, Burgess CM, et al (2020) Inactivation efficacy and mechanisms of

plasma activated water on bacteria in planktonic state. J Appl Microbiol 129:1248–1260. https://doi.org/10.1111/jam.14677

15. Hongzhuan Z, Ying T, Xia S, et al (2020) Preparation of the inactivated Newcastle disease vaccine by plasma activated water and evaluation of its protection efficacy. Appl Microbiol Biotechnol 104:107–117. https://doi.org/10.1007/s00253-019-10106-8

16. Kaushik NK, Ghimire B, Li Y, et al (2018) Biological and medical applications of plasma-activated media, water and solutions. Biol Chem 400:39–62. https://doi.org/10.1515/hsz-2018-0226

17. Xiang Q, Kang C, Niu L, et al (2018) Antibacterial activity and a membrane damage mechanism of plasma-activated water against Pseudomonas deceptionensis CM2. LWT 96:395–401. https://doi.org/10.1016/j.lwt.2018.05.059

18. Subramanian PSG, Jain A, Shivapuji AM, et al (2020) Plasma-activated water from a dielectric barrier discharge plasma source for the selective treatment of cancer cells. Plasma Process Polym 17:1900260. https://doi.org/10.1002/ppap.201900260

19. Ma R, Yu S, Tian Y, et al (2016) Effect of Non-Thermal Plasma-Activated Water on Fruit Decay and Quality in Postharvest Chinese Bayberries. Food Bioprocess Technol 9:1825–1834. https://doi.org/10.1007/s11947-016-1761-7

20. Li Y, Pan J, Ye G, et al (2017) In vitro studies of the antimicrobial effect of non-thermal plasma-activated water as a novel mouthwash. Eur J Oral Sci 125:463–470. https://doi.org/10.1111/eos.12374

21. Pan J, Li YL, Liu CM, et al (2017) Investigation of Cold Atmospheric Plasma-Activated

Water for the Dental Unit Waterline System Contamination and Safety Evaluation in Vitro. Plasma Chem Plasma Process 37:1091–1103. https://doi.org/10.1007/s11090-017-9811-0

22. Zhang Q, Ma R, Tian Y, et al (2016) Sterilization Efficiency of a Novel Electrochemical Disinfectant against Staphylococcus aureus. Environ Sci Technol 50:3184–3192. https://doi.org/10.1021/acs.est.5b05108

23. Sajib SA, Billah M, Mahmud S, et al (2020) Plasma activated water: the next generation eco-friendly stimulant for enhancing plant seed germination, vigor and increased enzyme activity, a study on black gram (Vigna mungo L.). Plasma Chem Plasma Process 40:119–143. https://doi.org/10.1007/s11090-019-10028-3

24. Tian Y, Ma R, Zhang Q, et al (2015) Assessment of the Physicochemical Properties and Biological Effects of Water Activated by Non-thermal Plasma Above and Beneath the Water Surface. Plasma Process Polym 12:439–449. https://doi.org/10.1002/ppap.201400082

25. Rathore V, Nema SK (2021) Optimization of process parameters to generate plasma activated water and study of physicochemical properties of plasma activated solutions at optimum condition. J Appl Phys 129:084901. https://doi.org/10.1063/5.0033848

26. ten Bosch L, Köhler R, Ortmann R, et al (2017) Insecticidal Effects of Plasma Treated Water. Int J Environ Res Public Health 14:1460. https://doi.org/10.3390/ijerph14121460

27. Ruamrungsri S, Sawangrat C, Panjama K, et al (2023) Effects of Using Plasma-Activated Water as a Nitrate Source on the Growth and Nutritional Quality of Hydroponically Grown Green Oak Lettuces. Horticulturae 9:248.

https://doi.org/10.3390/horticulturae9020248

28. Shen J, Tian Y, Li Y, et al (2016) Bactericidal Effects against S. aureus and Physicochemical Properties of Plasma Activated Water stored at different temperatures. Sci Rep 6:28505. https://doi.org/10.1038/srep28505

29. Box GE, Behnken DW (1960) Some new three level designs for the study of quantitative variables. Technometrics 2:455–475

30. Eisenberg G (1943) Colorimetric determination of hydrogen peroxide. Ind Eng Chem Anal Ed 15:327–328

31. Merino L (2009) Development and validation of a method for determination of residual nitrite/nitrate in foodstuffs and water after zinc reduction. Food Anal Methods 2:212–220

32. Khlyustova A, Labay C, Machala Z, et al (2019) Important parameters in plasma jets for the production of RONS in liquids for plasma medicine: A brief review. Front Chem Sci Eng 13:238–252. https://doi.org/10.1007/s11705-019-1801-8

33. Soni A, Choi J, Brightwell G (2021) Plasma-Activated Water (PAW) as a Disinfection Technology for Bacterial Inactivation with a Focus on Fruit and Vegetables. Foods 10:166. https://doi.org/10.3390/foods10010166

34. Xu Y, Tian Y, Ma R, et al (2016) Effect of plasma activated water on the postharvest quality of button mushrooms, Agaricus bisporus. Food Chem 197:436–444. https://doi.org/10.1016/j.foodchem.2015.10.144

35. Ghimire B, Szili EJ, Patenall BL, et al (2021) Enhancement of hydrogen peroxide production from an atmospheric pressure argon plasma jet and implications to the

antibacterial activity of plasma activated water. Plasma Sources Sci Technol 30:035009. https://doi.org/10.1088/1361-6595/abe0c9

36. Girard P-M, Arbabian A, Fleury M, et al (2016) Synergistic Effect of H2O2 and NO2 in Cell Death Induced by Cold Atmospheric He Plasma. Sci Rep 6:29098. https://doi.org/10.1038/srep29098

37. Norberg SA, Johnsen E, Kushner MJ (2015) Formation of reactive oxygen and nitrogen species by repetitive negatively pulsed helium atmospheric pressure plasma jets propagating into humid air. Plasma Sources Sci Technol 24:035026. https://doi.org/10.1088/0963-0252/24/3/035026

38. Risa Vaka M, Sone I, García Álvarez R, et al (2019) Towards the Next-Generation Disinfectant: Composition, Storability and Preservation Potential of Plasma Activated Water on Baby Spinach Leaves. Foods 8:692. https://doi.org/10.3390/foods8120692

39. Rayson MS, Mackie JC, Kennedy EM, Dlugogorski BZ (2012) Accurate Rate Constants for Decomposition of Aqueous Nitrous Acid. Inorg Chem 51:2178–2185. https://doi.org/10.1021/ic202081z

40. Xiang Q, Zhang R, Fan L, et al (2020) Microbial inactivation and quality of grapes treated by plasma-activated water combined with mild heat. LWT 126:109336. https://doi.org/10.1016/j.lwt.2020.109336

41. Tsoukou E, Bourke P, Boehm D (2020) Temperature Stability and Effectiveness of Plasma-Activated Liquids over an 18 Months Period. Water 12:3021. https://doi.org/10.3390/w12113021

Figure Captions

Figure 1. Schematic of the plasma unit used for the preparation of PAW.

Figure 2. Response surface and contour plots showing the effects of He flow rate, distance of the glass tube nozzle from the water surface, volume of the water, discharge voltage, and treatment time on H_2O_2 concentration of PAW. Effect of (a) He flow rate and distance of the glass tube nozzle from the water surface, (b) volume of the water and discharge voltage, (c) treatment time and He flow rate, and (d) treatment time and discharge voltage.

Figure 3. Response surface and contour plots showing the effects of He flow rate, distance of the glass tube from the water surface, volume of the water, discharge voltage, and treatment time on NO_2^- concentration of PAW. Effect of (a) He flow rate and distance of the glass tube nozzle from the water surface, (b) volume of the water and discharge voltage, (c) treatment time and He flow rate, and (d) treatment time and discharge voltage.

Figure 4. Response surface and contour plots showing the effects of He flow rate, distance of the glass tube nozzle from the water surface, volume of the water, discharge voltage, and treatment time on NO_3^- concentration of PAW. Effect of (a) He flow rate and distance of the glass tube

nozzle from the water surface, (b) volume of the water and discharge voltage, (c) treatment time and He flow rate, and (d) treatment time and discharge voltage.

Figure 5. Response surface and contour plots showing the effects of He flow rate, distance of the glass tube from the water surface, volume of the water, discharge voltage, and treatment time on pH of PAW. Effect of (a) He flow rate and distance of the glass tube nozzle from the water surface, (b) volume of the water and discharge voltage, (c) treatment time and He flow rate, and (d) treatment time and discharge voltage.

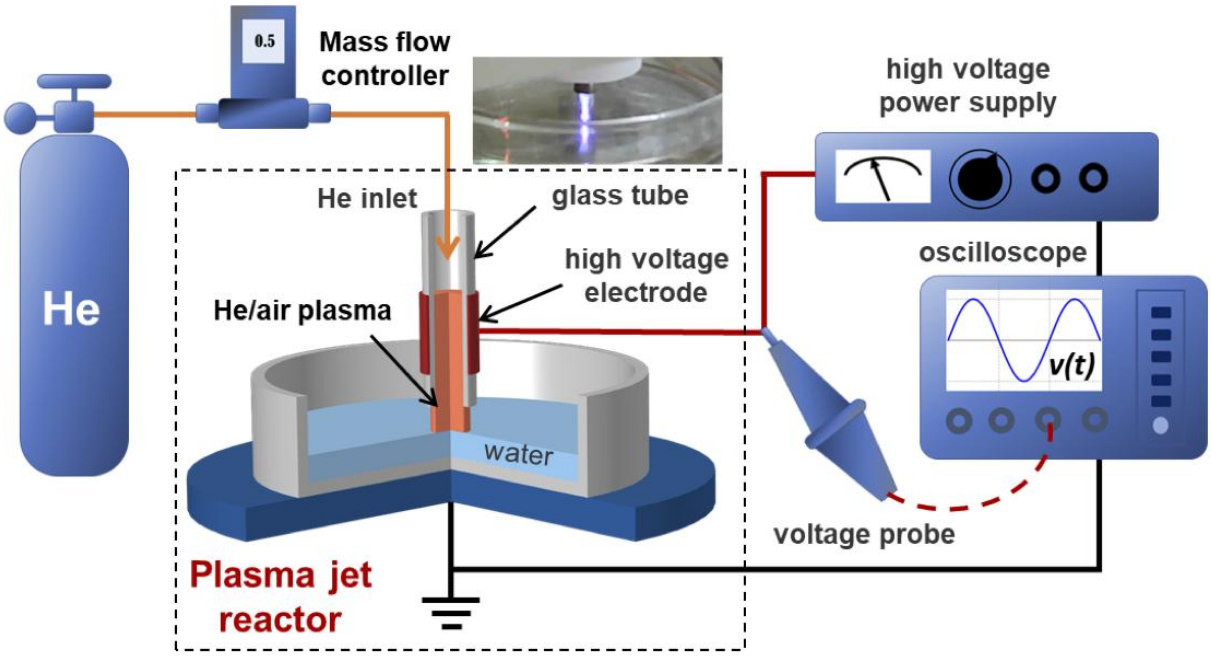
Figure 6. Response surface and contour plots showing the effects of He flow rate, distance of the glass tube nozzle from the water surface, volume of the water, discharge voltage and treatment time on EC of PAW. Effect of (a) He flow rate and distance of the glass tube nozzle from the water surface, (b) volume of the water and discharge voltage, (c) treatment time and He flow rate, and (d) treatment time and discharge voltage.

Figure 7. H_2O_2 concentration vs. storage time during a 105-day storage period at (a) 25, 10, 4, and 0°C and (b) -12, -18, -24, and -80°C. Error bars represent the standard deviation of triplicates. Lines represent the fitting of Equation (2) on experimental data.

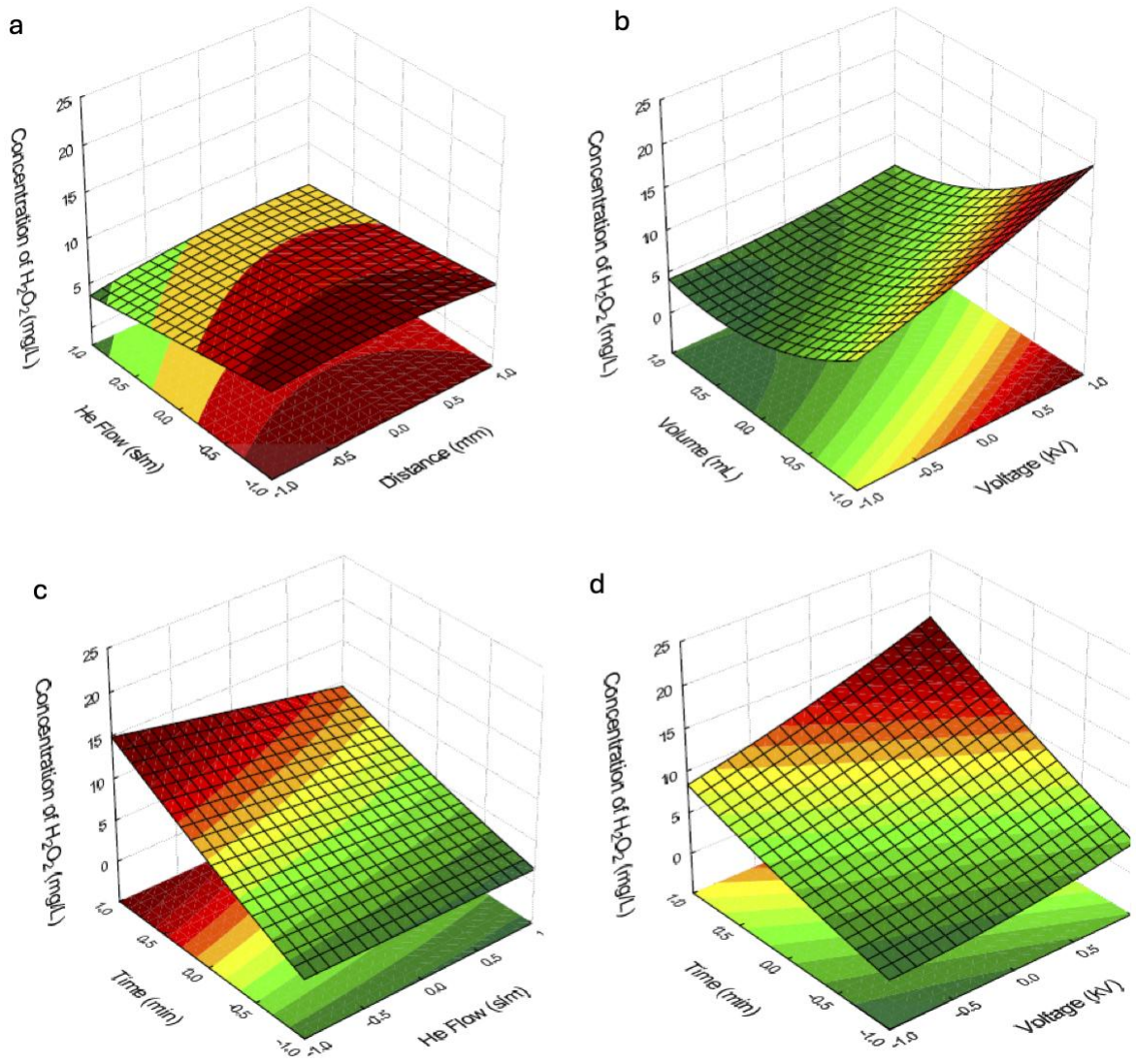
Figure 8. NO_2^- concentration in PAW vs storage time during a 105-day storage period at (a) 25, 10, 4, and 0 °C and (b) -12, -18, -24, and -80°C. Error bars represent the standard deviation of triplicates. Lines represent the fitting of Equation (2) on experimental data.

Figure 9. NO_3^- concentration in PAW vs storage time during a 105-day storage period at (a) 25, 10, 4, and 0 °C and (b) -12, -18, -24, and -80°C. Error bars represent the standard deviation of triplicates. Lines represent the fitting of Equation (2) on experimental data.

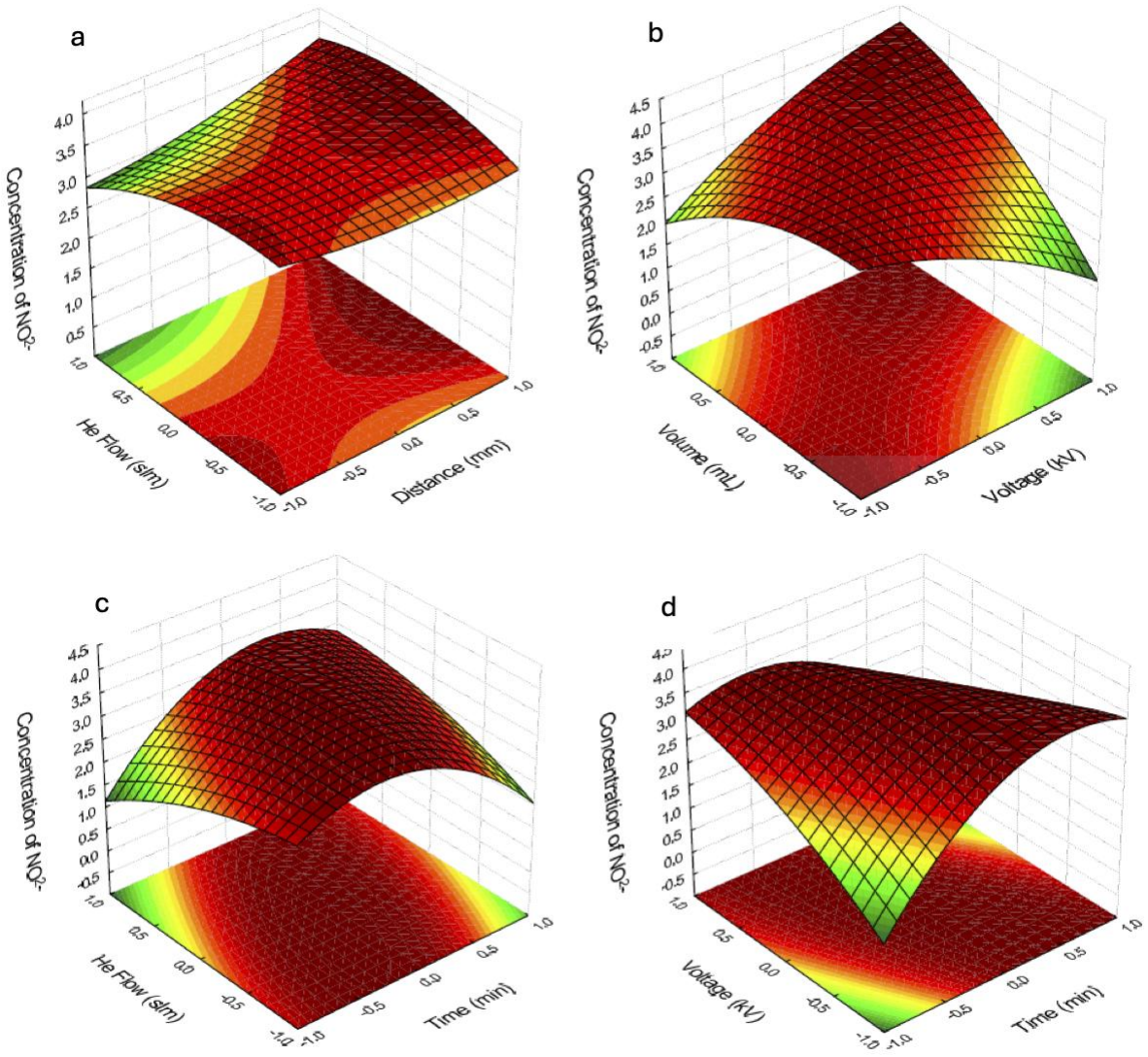
Figure 10. Correlation of predicted and observed values for H_2O_2, NO_2^-, and NO_3^- concentrations in PAW. The predicted values for H_2O_2, NO_2^-, and NO_3^- concentration in PAW during refrigerated and freezer storage were fitted to Equations 10-15, respectively.


0.5
Mass flow controller
high voltage power supply
He
He inlet
glass tube
high voltage electrode
oscilloscope
He/air plasma
v(t)
water
voltage probe
Plasma jet reactor

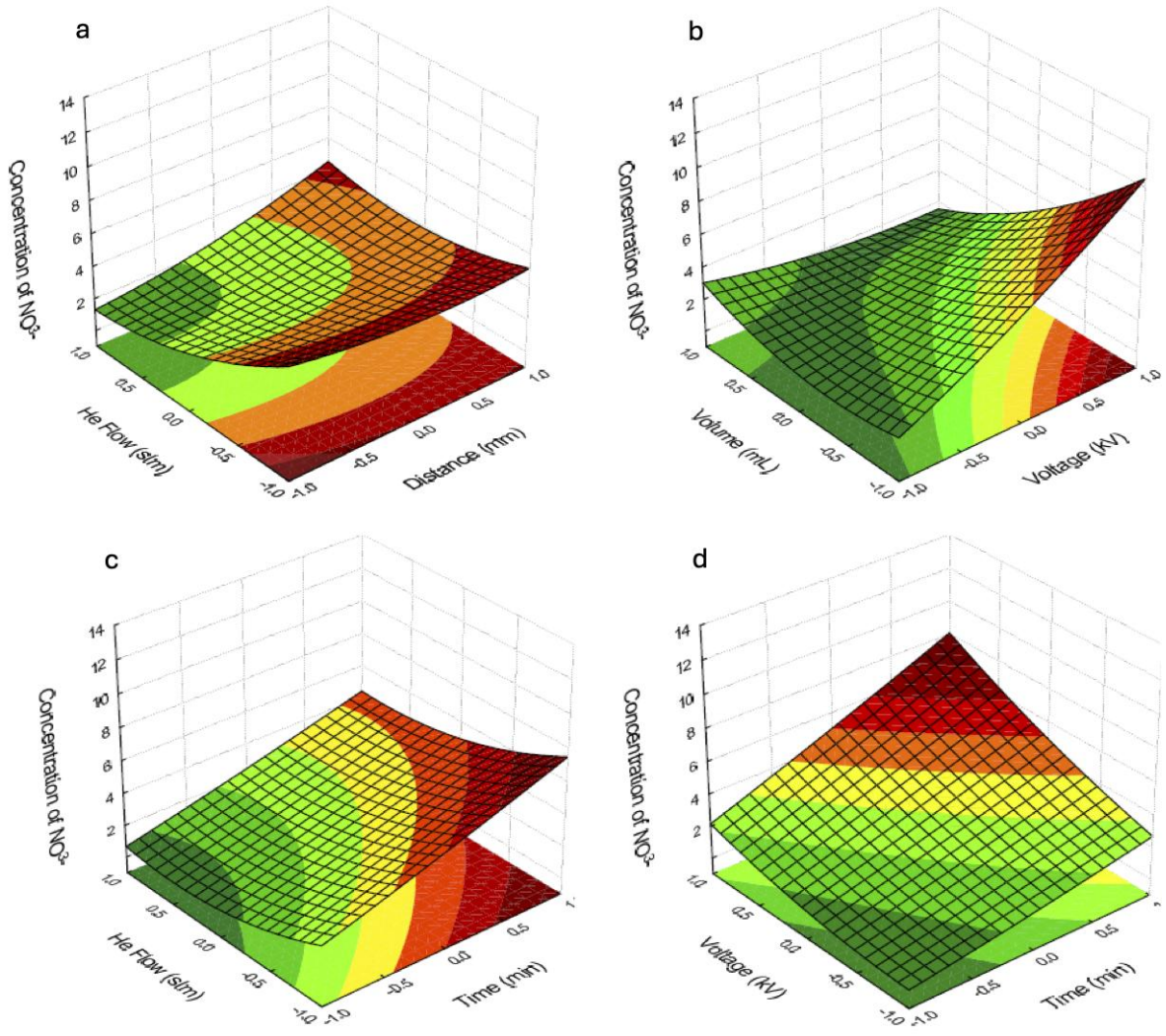
835


a
Concentration of H_2O_2 (mg/L)
25
20
15
10
5
He Flow (slm)
1.0
0.5
0.0
-0.5
-1.0
Distance (mm)
b
Concentration of H_2O_2 (mg/L)
25
20
15
10
5
0
Volume (mL)
Voltage (kV)
c
Concentration of H_2O_2 (mg/L)
Time (min)
He Flow (slm)
d
Concentration of H_2O_2 (mg/L)
Time (min)
Voltage (kV)

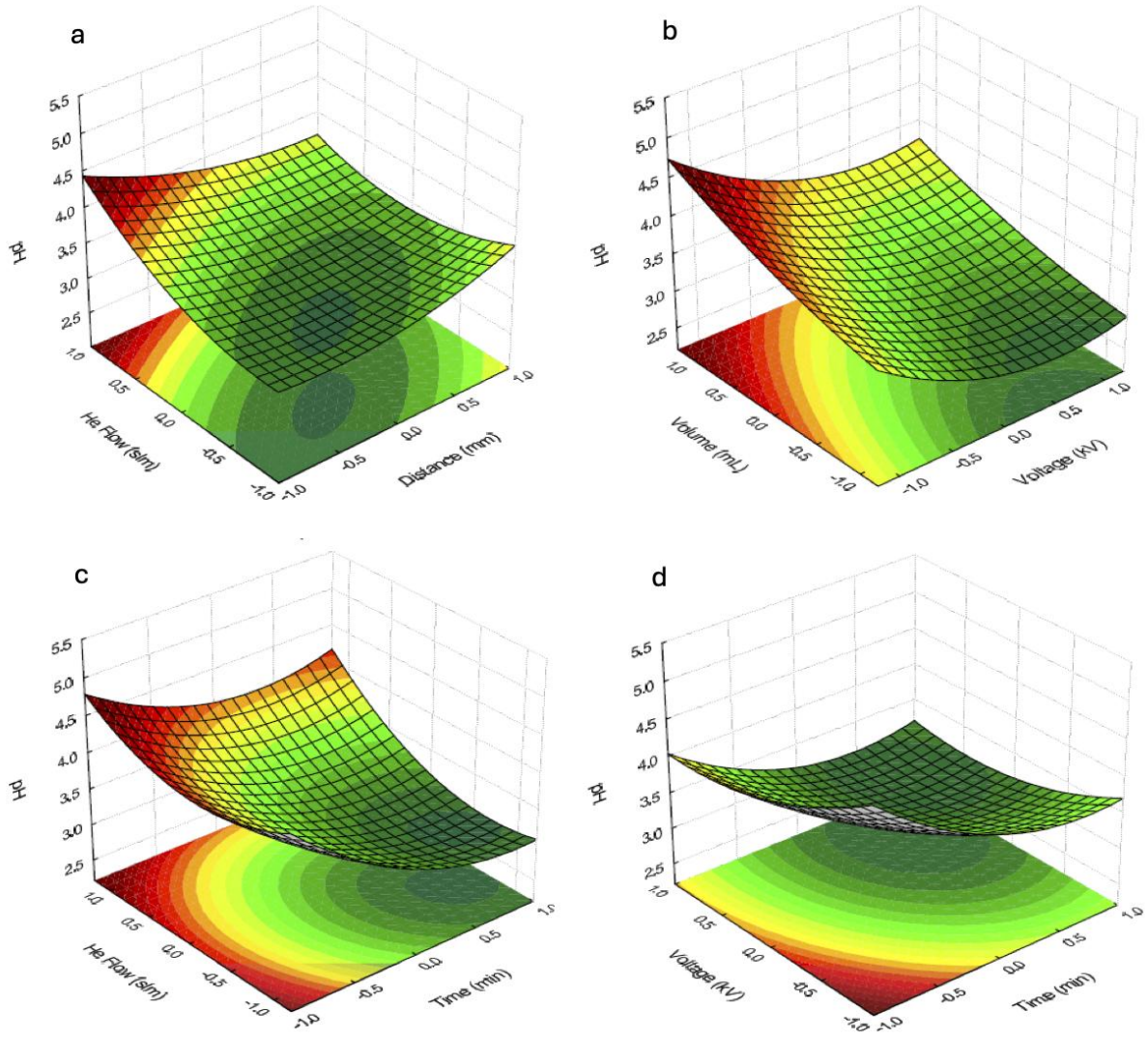
836


a
Concentration of NO2-
He Flow (slm)
Distance (mm)
b
Concentration of NO2-
Volume (mL)
Voltage (kV)
c
Concentration of NO2-
He Flow (slm)
Time (min)
d
Concentration of NO2-
Voltage (kV)
Time (min)

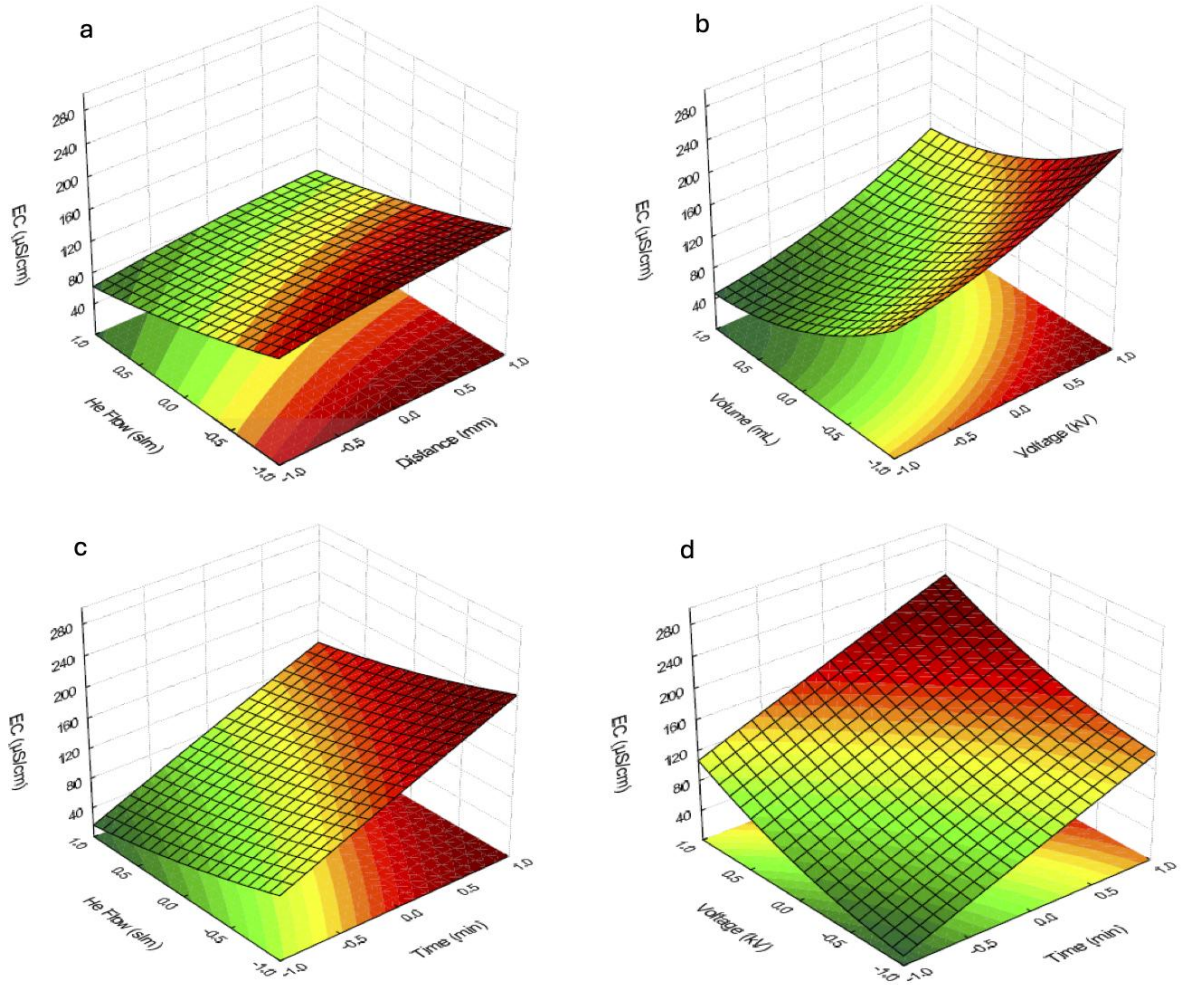
837


a
Concentration of NO3-
He Flow (slm)
Distance (mm)
b
Concentration of NO3-
Volume (mL)
Voltage (kV)
c
Concentration of NO3-
He Flow (slm)
Time (min)
d
Concentration of NO3-
Voltage (kV)
Time (min)

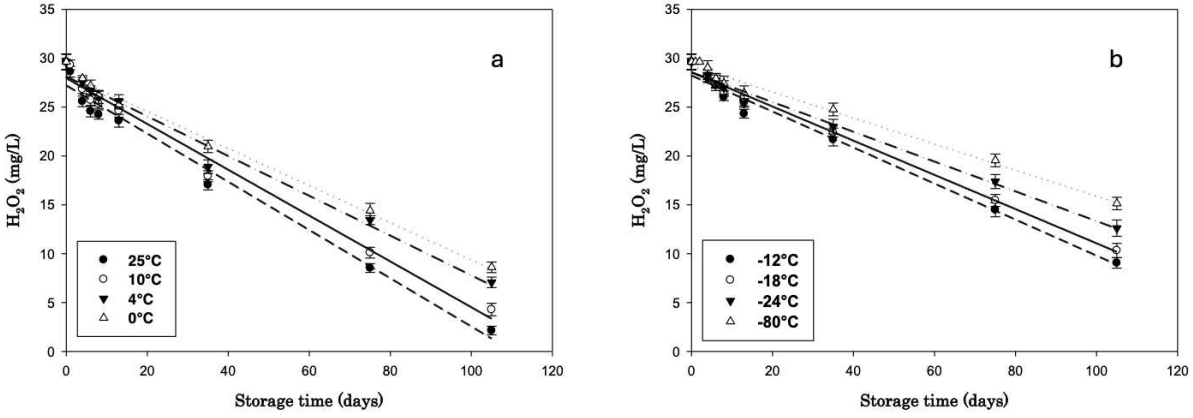
838


a
pH
5.5
5.0
4.5
4.0
3.5
3.0
2.5
He Flow (slm)
1.0
0.5
0.0
-0.5
-1.0
Distance (mm)
b
Volume (mL)
Voltage (kV)
c
Time (min)
d

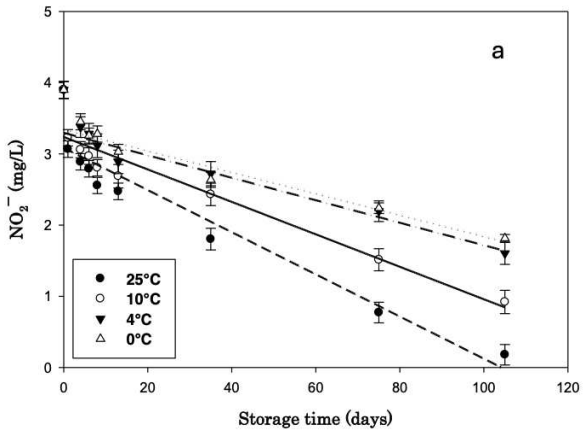
839

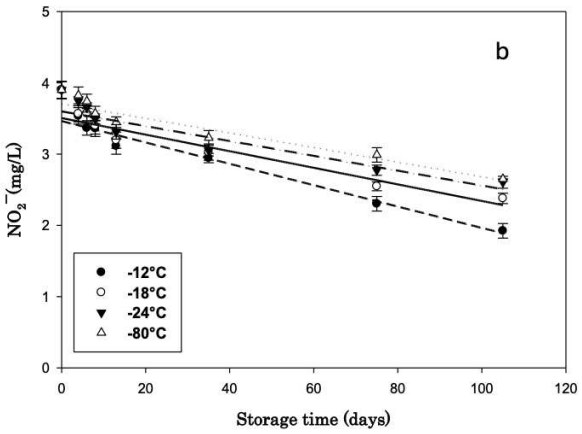

a
EC (µS/cm)
He Flow (slm)
Distance (mm)
b
Volume (mL)
Voltage (kV)
c
Time (min)
d

840

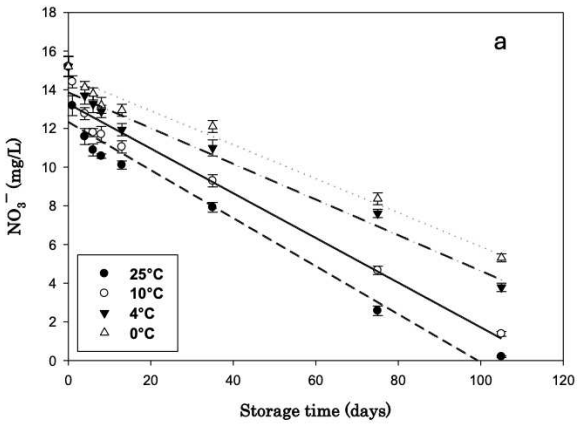

a
H_2O_2 (mg/L)
25°C
10°C
4°C
0°C
Storage time (days)
b
-12°C
-18°C
-24°C
-80°C

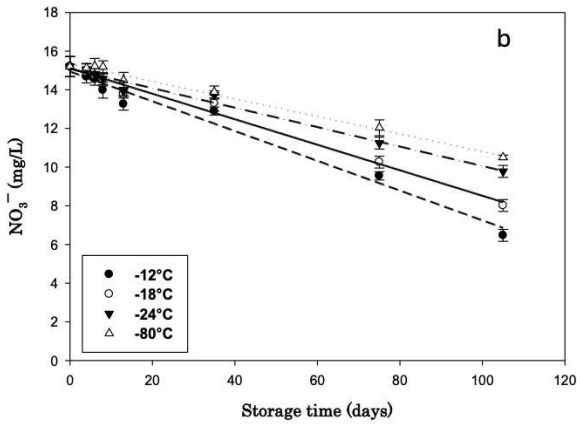
841


a
NO_2^- (mg/L)
Storage time (days)
25°C
10°C
4°C
0°C


b
NO_2^- (mg/L)
Storage time (days)
-12°C
-18°C
-24°C
-80°C

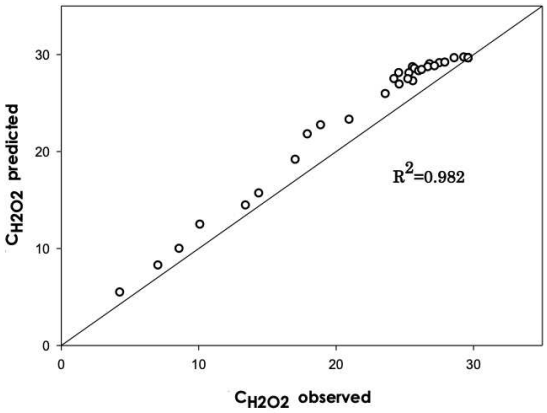
842

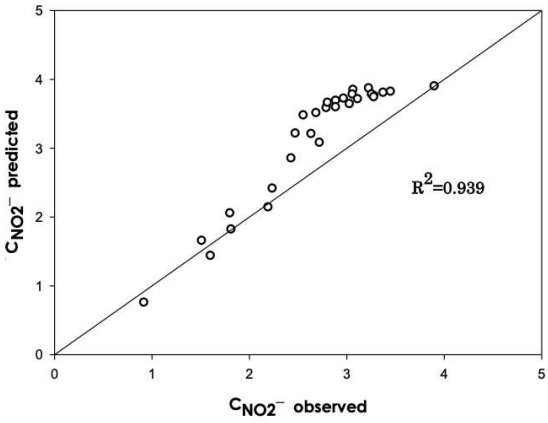

a
NO_3^- (mg/L)
Storage time (days)
25°C
10°C
4°C
0°C

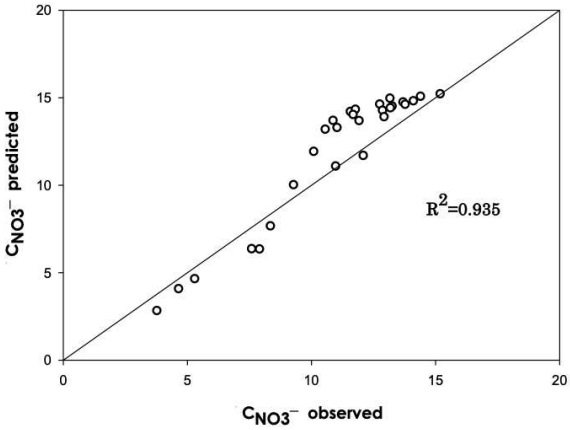

b
NO_3^- (mg/L)
Storage time (days)
-12°C
-18°C
-24°C
-80°C

843

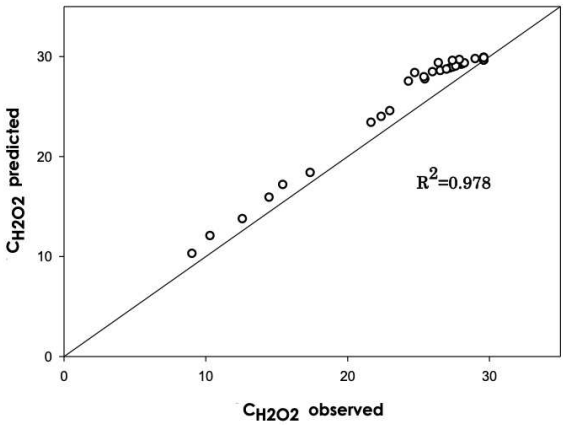
Refrigerated storage (0-25°C)

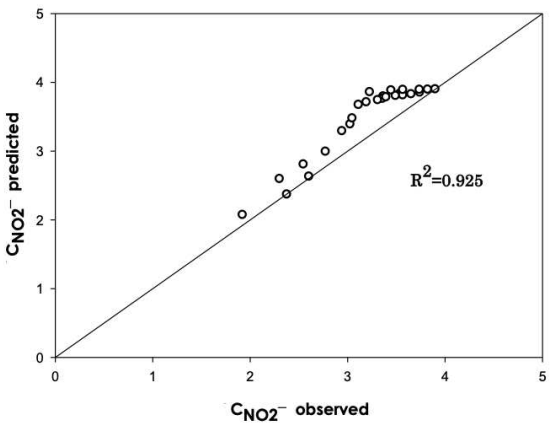


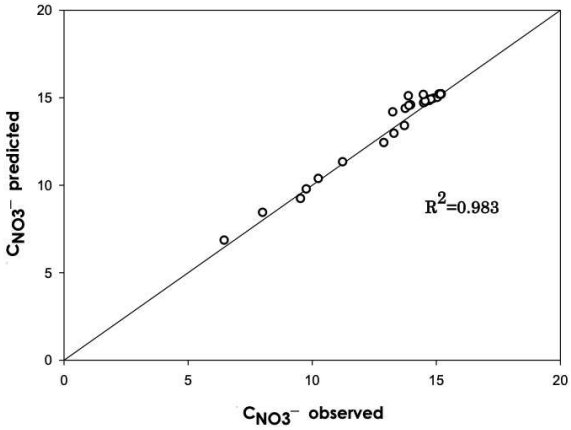




Freezer storage (–12—80°C)







844